



Swansea University
Prifysgol Abertawe



Cronfa - Swansea University Open Access Repository

This is an author produced version of a paper published in :
Remote Sensing of Environment

Cronfa URL for this paper:
<http://cronfa.swan.ac.uk/Record/cronfa32733>

Paper:

Hernández-Clemente, R., North, P., Hornero, A. & Zarco-Tejada, P. (2017). Assessing the effects of forest health on sun-induced chlorophyll fluorescence using the FluorFLIGHT 3-D radiative transfer model to account for forest structure. *Remote Sensing of Environment*, 193, 165-179.
<http://dx.doi.org/10.1016/j.rse.2017.02.012>

This article is brought to you by Swansea University. Any person downloading material is agreeing to abide by the terms of the repository licence. Authors are personally responsible for adhering to publisher restrictions or conditions. When uploading content they are required to comply with their publisher agreement and the SHERPA RoMEO database to judge whether or not it is copyright safe to add this version of the paper to this repository.
<http://www.swansea.ac.uk/iss/researchsupport/cronfa-support/>

1 **Assessing the effects of forest health on sun-induced chlorophyll fluorescence using the**
2 **FluorFLIGHT 3-D radiative transfer model to account for forest structure**

3 R. Hernández-Clemente^{1*}, P.R.J. North¹, A. Hornero², P.J. Zarco-Tejada³

4
5 ¹Department of Geography, Swansea University, SA2 8PP, Swansea, UK.

6 ²Instituto de Agricultura Sostenible (IAS), Consejo Superior de Investigaciones Científicas (CSIC), Córdoba,
7 Spain

8 ³European Commission, Joint Research Centre (JRC), Directorate D – Sustainable Resources - Bio-Economy
9 Unit, Via E. Fermi 2749 – TP 261, 26a/043, I-21027 Ispra (VA), Italy

10
11
12
13 *Corresponding author:

14
15 Rocío Hernández Clemente
16 Department of Geography
17 Swansea University
18 SA2 8PP- Swansea,
19 UK
20 Tel: +44 1792 295860
21 Fax: +44 1792 295110
22 e-mail: r.hernandez-clemente@swansea.ac.uk
23 <http://orcid.org/0000-0002-4434-8346>
24
25
26
27
28
29

30 Submitted to *Remote Sensing of Environment*
31 August 2016
32

33 **Abstract**

34 Sun-induced fluorescence (SIF) has been proven to serve as a proxy of photosynthesis
35 activity and therefore, as an early indicator of physiological alterations for global monitoring
36 of vegetation. However, the interpretation of SIF over different spatial resolutions is critical
37 to bridge the existing gap between local and global scales. This study provides insight into
38 the influence of scene components, and forest structure and composition on the quantification
39 of the red and far-red fluorescence signal as an early indicator of forest decline. The
40 experiments were conducted over an oak forest (*Quercus ilex*) affected by water stress and
41 *Phytophthora* infection in the southwest of Spain. SIF retrievals through the Fraunhofer Line
42 Depth (FLD) principle with three spectral bands F (FLD3) was assessed using high resolution
43 (60 cm) hyperspectral imagery extracting sunlit crown, full crown and aggregated pixels.
44 Results showed the link between F (FLD3) extracted from sunlit crown pixels and the tree
45 physiological condition in this context of disease infection, yielding significant relationships
46 ($r^2=0.57$, $p<0.01$) for midday xylem water potential (ψ), ($r^2=0.63$, $p<0.001$) for the de-
47 epoxidation state of the xanthophyll cycle (DEPS), and ($r^2=0.74$, $p<0.001$) for leaf-level
48 measurements of steady-state fluorescence yield (F_s). In contrast, a poor relationship was
49 obtained when using aggregated pixels at 30 m spatial resolution, where the relationship
50 between the image-based F (FLD3) and F_s yielded a non-significant relationship ($r^2=0.25$,
51 $p>0.05$). These results demonstrate the need for methods to accurately retrieve crown SIF
52 from aggregated pixels in heterogeneous forest canopies with large physiological variability
53 among individual trees. This aspect is critical where structural canopy variations and the
54 direct influence of background and shadows affect the SIF amplitude masking the natural
55 variations caused by physiological condition. FluorFLIGHT, a modified version of the three
56 dimensional (3-D) radiative transfer model FLIGHT was developed for this work, enabling
57 the simulation of canopy radiance and reflectance including fluorescence at different spatial

58 resolutions, such as may be derived from proposed satellite missions such as FLEX, and
59 accounting for canopy structure and varying percentage cover. The 3-D modelling approach
60 proposed here significantly improved the relationship between F_s and F (FLD3) extracted
61 from aggregated pixels ($r^2=0.70$, $p<0.001$), performing better than when aggregation effects
62 were not considered ($r^2=0.42$, $p<0.01$). The FluorFLIGHT model used in this study improved
63 the retrieval of SIF from aggregated pixels as a function of fractional cover, leaf area index
64 and chlorophyll content yielding significant relationships between F_s ground-data
65 measurements and fluorescence quantum yield estimated with FluorFLIGHT at $p<0.01$
66 ($r^2=0.79$). The methodology presented here using FluorFLIGHT also demonstrated its
67 capabilities for mapping SIF at the tree level for single tree assessment of forest physiological
68 condition in the context of early disease detection.

69 ***Keywords***

70 Fluorescence, stress detection, hyperspectral, SIF, RTM, forest dieback, oak forest,
71 *Phytophthora* infection.

72

73 **1. Introduction**

74 Spatial and temporal estimation of photosynthesis of forest ecosystems can provide advance
75 information on plant performance and forest dynamics in a given environment. Sun-induced
76 chlorophyll fluorescence (SIF) has been extensively tested as a proxy of fundamental
77 processes of plant physiology to understand the photosynthetic activity of plants and the
78 stress development affecting photochemistry (Damm et al., 2014; Krause and Weis, 1984;
79 Zarco-Tejada et al., 2013a). Current research efforts to monitor photosynthetic activity show
80 a growing interest in remote sensing of the SIF signal due to its potential to be measured at

81 both local (high resolution images) and global scales (medium and low resolution images)
82 being a direct proxy of photosynthesis. The first global maps of SIF were published
83 (Frankenberg et al., 2011; Joiner et al., 2014) using the TANSO sensor on board GOSAT
84 (Kuze et al., 2009) allowing qualitative assessments with annual and seasonal vegetation
85 patterns (Guanter et al., 2012). The spatial resolution provided by this sensor (10.5 km) is not,
86 however, sufficient for the understanding of the retrieved SIF in heterogeneous vegetation
87 canopies due to the aggregation of scene components and the large effects caused by
88 background and shadows (Zarco-Tejada et al., 2013b). The fast development of new
89 hyperspectral sensors to be carried on board manned and unmanned airborne platforms has
90 given rise to the retrieval of high spatial resolution SIF at local scales, which is becoming a
91 novel area of research (Damm et al., 2015; Zarco-Tejada et al., 2013c). However it remains
92 very challenging to cover at very high resolution the large areas required for forest
93 monitoring analysis. This has hitherto been the main limitation in studying physiological
94 condition of forest canopies with higher detail, as currently available satellite sensors are
95 limited by their spatial and spectral resolution for SIF retrieval purposes. To address this gap,
96 the ESA's Earth Explorer Mission of the 'Fluorescence Explorer' (FLEX) (Kraft et al., 2012),
97 the first mission designed to observe the photosynthetic activity of the vegetation layer has
98 been recently approved, with 2022 as the tentative launch date. This mission will make
99 possible, for the first time, the assessment of the dynamics of photosynthesis on forest
100 canopies through SIF at 300 m spatial resolution, and with potential to distinguish different
101 fluorescence signals from PSI and PSII (Rossini et al., 2015). This offers a great advantage
102 over current techniques used for photosynthesis monitoring based on structural indices (e.g.
103 the Normalized Difference Vegetation Index (NDVI)) acquired from conventional Earth-
104 resource satellites.

105 The chlorophyll fluorescence signal derived from global maps is affected by illumination
106 effects, leaf and canopy structure and composition of vegetation, and soil / background
107 though to a lesser extent than reflectance. The interplay of within-leaf scattering properties of
108 leaf structure and biochemical constituents are known to affect the bidirectional chlorophyll
109 fluorescence emission (Van Wittenberghe et al., 2015, 2014; Verrelst et al., 2015). SIF flux
110 through a leaf, upward and downward leaf chlorophyll fluorescence emissions and scattering
111 effects have been thoroughly studied using radiative transfer models (RTMs) (Miller, 2005).
112 However, few fluorescence models have been developed at the leaf level and even fewer are
113 available at the canopy level, especially for the case of heterogeneous and complex canopies.
114 The first attempts were carried as part of a vegetation fluorescence canopy model developed
115 in the framework of the ESTEC ESA project (16365/02/NL/FF). The FluorMODleaf (Pedrós
116 et al., 2008) and FluorSAIL (Verhoef, 2004) leaf and canopy fluorescence models were
117 developed within the same project. FluorMODleaf is based on the widely used and validated
118 PROSPECT leaf optical properties model and requires inputs from PROSPECT-5 plus the
119 σ_{II}/σ_I ratio referring to the relative absorption cross-sections of PSI and PSII, as well as the
120 fluorescence quantum efficiency of PSI and PSII, represented by the corresponding mean
121 fluorescence lifetimes τ_I and τ_{II} . The canopy model is based on the turbid medium SAIL
122 model (FluorSAIL) coupled with FluorMODleaf and MODTRAN to provide the illumination
123 levels through the canopy. The Soil Canopy Observation, Photochemistry and Energy fluxes
124 (SCOPE) model recently developed by van der Tol et al., (2009) as a means of jointly
125 simulating directional Top of Canopy (TOC) reflected solar radiation, emitted thermal
126 radiation and SIF signals as well as energy balance, water and CO₂ fluxes, enables vertical
127 (1-D) modelling of integrated radiative transfer and energy balance by combining a number
128 of intra-canopy radiative, turbulent and mass-transfer models, bearing in mind various
129 processes involved in leaf biochemistry (Duffour et al., 2015). Using retrievals of SIF

130 simulated with SCOPE, Verrelst et al. (2015) demonstrated that the main variables affecting
131 SIF signal were determined by leaf optical properties and canopy structural variables with a
132 contribution of 77.9% of the SIF total variability. Canopy re-absorption and scattering effects
133 must be better understood and quantified. Consequently, it is very important to make progress
134 on canopy-scale modelling approaches providing an explicit connection between the canopy
135 biophysical processes, view and illumination geometry and the resulting canopy fluorescence
136 signal. In light of the above, Zarco-Tejada et al. (2013b) demonstrated the need for RTM
137 methods to accurately retrieve vegetation fluorescence signal from vegetation-
138 soil/background aggregated pixels. Due to the lack of complex models to simulate SIF in
139 heterogeneous canopies, Zarco-Tejada and co-authors conducted the study using a leaf-
140 canopy fluorescence model (FluorMODleaf) combined with a geometric model to account for
141 canopy heterogeneity (FluorSAIL) and a first-order approximation forest model (FLIM) of
142 stand reflectance to account the effects of crown transparency and shadowing on apparent
143 reflectance. The results demonstrated the large structural effects on the fluorescence retrieval
144 from mixed pixels, and therefore the need to develop more complex models to account for the
145 effect caused by the canopy architecture.

146 This aspect becomes particularly important in the assessment of complex forest canopies
147 characterised by high horizontal and vertical heterogeneity (Widłowski et al., 2015).
148 Unfortunately, currently available fluorescence models are only valid on homogeneous and
149 uniform canopies. Strategies to simulate the spectral signature in heterogeneous forest
150 canopies have been limited by difficulties in simulating canopy structure such as Leaf Area
151 Index (LAI), tree density, fractional cover (FC), crown overlapping or mutual shading and
152 multiple scattering between crowns. This paper aims to fill these gaps and in doing so to
153 assess the potential of chlorophyll fluorescence signal retrieval as an early indicator of forest
154 decline. The novel approach consists of coupling the leaf optical model FLUSPECT (Vilfana

155 et al., 2016) and the three-dimensional (3-D) ray-tracing model FLIGHT developed by North,
156 (1996) to carry the scaling up approach from leaf to canopy dealing with multiple canopy
157 components. In particular, the study aims at assessing: i) SIF as an early indicator of forest
158 health in a heterogeneous oak forest canopy (*Quercus ilex*) affected by water stress and
159 *Phytophthora* infection using very high resolution airborne hyperspectral imagery, ii) the
160 canopy structure effects on the retrieval of SIF in forest canopies using a 3-D RTM, and iii)
161 the retrieval of SIF through model inversion using coarse-spatial resolution hyperspectral
162 imagery.

163

164 **2. Materials and methods.**

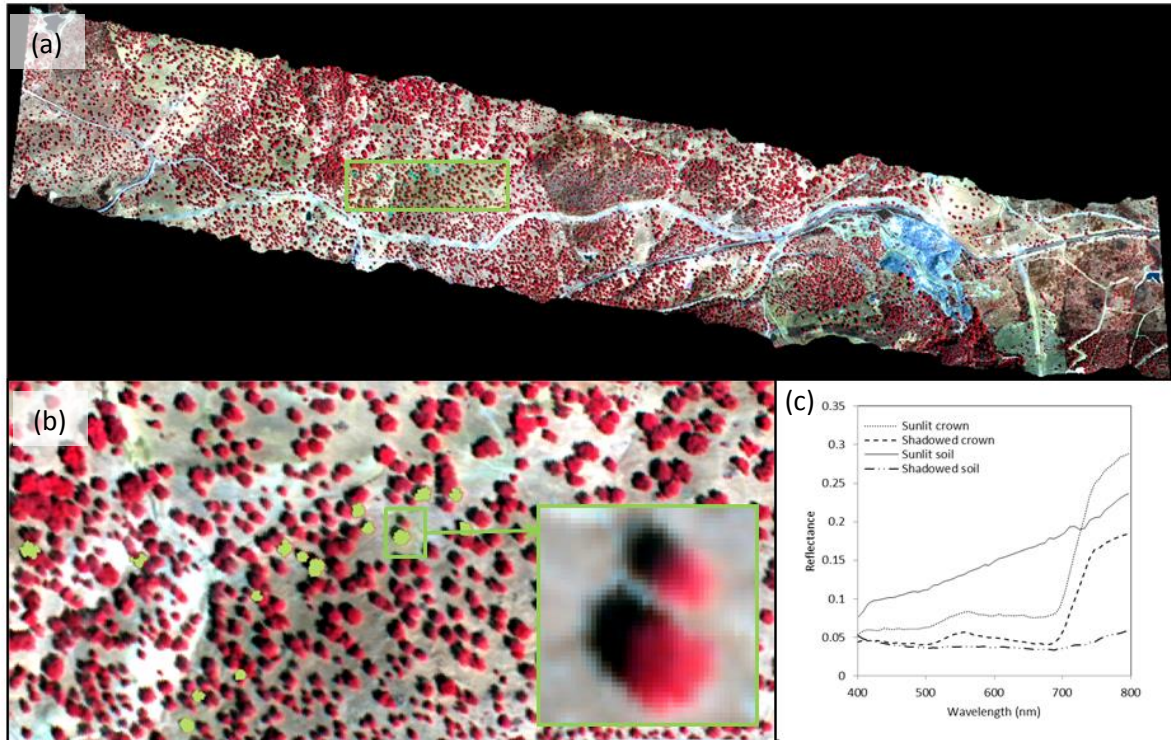
165 The methods used for the assessment of SIF from hyperspectral imagery for the early
166 detection of forest decline condition are described below, outlining field and airborne data
167 collection, as well as the approach using the 3-D RTM FLIGHT adapted to account for
168 fluorescence (FluorFLIGHT). In both cases, SIF was retrieved within the far-red region.

169 **2.1. Field data collection.**

170 The experimental area is located in Puebla de Guzmán (Huelva province, in southwestern
171 Spain) (Lat 37°36'30.89"N, Lon 7°20'27.97"W) (Fig. 1). The topography is slightly hilly,
172 with acidic and poor soils. The annual rainfall is around 490 mm with an annual average
173 temperature of 18.1 °C, reaching an annual average of 32 °C during summer and an annual
174 average of 12.7 °C during winter. The vegetation is mainly composed of mature trees of the
175 species *Quercus ilex* subsp. Bellota with an average density of 60 trees per ha (Roig Gómez
176 et al., 2007). Since the 1990s, trees have shown symptoms of decline, leading to high
177 mortality rates from the 2000s (Maurel et al., 2001). This region is particularly vulnerable
178 because of the combined effect of water deficiency, soil compaction, nutrient losses, water

179 erosion and the widespread distribution of soil-borne pathogen (*Pytophthora cinnamomi* and
180 *Pythiumspiculum*) (Moralejo et al., 2009).

181



182

183 **Fig. 1.** Airborne hyperspectral flight line acquired with the micro-hyperspectral imager yielding 60
184 cm resolution (a), oak forest study site and tree crowns selected for the quantification of SIF (b), high
185 resolution spectral reflectance extracted from sunlit and shadowed crown and soil components (c).

186

187 The field data measurements were conducted in 15 oak trees (*Quercus ilex* subsp. Bellota)
188 with similar height and age located in low slope areas (< 10%). The location of these trees
189 was previously associated with the pathogenicity of *P. cinmaomi* (Ferraz et al., 2000) and
190 heat-induced tree die-off processes (Natalini et al., 2016). The trees were selected to ensure a
191 gradient in health condition based on the physiological variables: de-epoxidation of the
192 xanthophyll cycle (DEPS), midday xylem water potential (ψ) and steady-state fluorescence
193 yield (F_s). Three different forest physiological conditions (FPC-1,2,3) were established based

194 on these variables, where FPC1 correspond with the healthier and more vigorous trees, FPC2
195 with moderated affected trees, and FPC3 with declining trees. In order to determine whether
196 FPCs differed significantly in terms of DEPS, ψ and F_s , a one-way ANOVA was performed
197 at a 0.05 significance level. Findings indicated significant differences in physiological status
198 for each FPC ($p < 0.05$). A similar procedure was used by Hernández-Clemente et al. (2011)
199 to established physiological condition levels in a conifer forest affected by water stress.

200 A summary of the variables measured in the field is included in Table 1. Physiological
201 measurements were carried out concurrently with the airborne measurements (12:00 to 13:00
202 h local time) during three consecutive days (25-28 August in 2012). ψ was measured with a
203 pressure chamber (SKPM 1400, Skye Instruments Ltd, Powys, UK) (Scholander et al., 1965)
204 from 12 branches per tree, three branches per orientation in the four cardinal directions. F_s
205 was measured on five leaves per orientation and tree, with a total of 300 leaves sampled. Leaf
206 fluorescence was measured using a FluorPen FP100 (Photon Systems Instruments, Brno,
207 Czech Republic), which was self-calibrated at the start of each session. Although
208 measurements made with the FluorPen FP100 differed from airborne SIF retrievals, leaf data
209 served as a field-level assessment of variability in stress conditions (Zarco-Tejada et al.,
210 2016).

211 Leaf biochemical constituents measured from the selected trees were total chlorophyll (C_{a+b})
212 (chlorophyll a (C_a) and chlorophyll b (C_b)), total carotenoids (C_{x+c}) and xanthophyll
213 pigments, and leaf water content (C_w) and dry mass (C_s). Leaf-level measurements were
214 collected on a total of 48 leaves per tree, 12 samples per orientation, with a total of 720 leaves
215 sampled. The samples were collected from the top of the crown by selecting branches of
216 illuminated areas. Leaf pigments were processed and extracted as reported by Hernandez-
217 Clemente et al. (2011). The DEPS was calculated as $(A+Z)/(A+V+Z)$ (Thayer & Björkman,
218 1990), where V is violaxanthin, A is antheraxanthin and Z is zeaxanthin.

219 Optical measurements were taken on leaves from the same branches and trees used for
 220 pigment quantification. Leaf reflectance (ρ) and transmittance (τ) were measured with a Li-
 221 Cor 1800-12 integrating sphere (Li-Cor, Lincoln, NE, USA) coupled to a fiber optic
 222 spectrometer (Ocean Optics model USB2000 spectrometer, Ocean Optics, Dunedin, FL,
 223 USA), with a 1024-element detector array, 0.5 nm sampling interval, and 7.5 nm spectral
 224 resolution in the 340–940 nm range using the method described in Zarco-Tejada et al. (2005).

225

226 **Table 1.**

227 Ground truth data collected and optical measurements.

Variable	Symbol	Units
<i>Biochemical constituents & physiological variables</i>		
Chlorophyll content	C_{a+b}	$\mu\text{g}/\text{cm}^2$
Carotenoid content	C_{x+c}	$\mu\text{g}/\text{cm}^2$
Water content	C_w	mg/cm^2
Dry matter	C_m	mg/cm^2
Xanthophyll cycle	DEPS	arbitrary units
Steady State Fluorescence	Fs	arbitrary units
Water potential	ψ	mpa
<i>Optical measurements</i>		
Leaf reflectance	ρ	%
Leaf transmittance	τ	%
Solar irradiance	I_o	$\text{wm}^{-2}\text{sr}^{-1}\text{nm}^{-1}$
<i>Forest canopy structure</i>		
Density	D	trees/ha
Trunk diameter	\emptyset_t	m
Tree height	H	m
Crown diameter	\emptyset_c	m
Crown height	H_c	m
Leaf Area Index	LAI	m^2/m^2

228

229

230 In February 2013, the study area was inventoried recording the main structural variables of
 231 the canopy. A total of 200 trees were measured recording the trunk diameter at 1.3 m, tree
 232 height, crown diameter, tree density, FC and height. Additionally, LAI values were taken

233 from a subsample of 15 trees of this data set. A detailed description of the measurement
234 procedure can be found in Hernandez-Clemente et al. (2014).

235 **2.2. Airborne image acquisitions**

236 The airborne campaign was conducted with a hyperspectral sensor installed on an aircraft
237 (CESSNA C172S EC-JYN) operated by the Laboratory for Research Methods in Quantitative
238 Remote Sensing (QuantaLab), Consejo Superior de Investigaciones Científicas (IAS-CSIC,
239 Spain) at 650-700 m above ground level (AGL) and 2800 ft. above the sea level (ASL). The
240 images were acquired concurrent with field data acquisitions on 28 August 2012 between
241 11:30 and 13:00, local time.

242 The images were collected with a visible and near-infrared (VNIR) micro-hyperspectral
243 imager (Micro-Hyperspec VNIR model, Headwall Photonics, MA, USA). The sensor was
244 configured in the spectral mode of 260 bands at 1.85 nm/pixel and 12-bit radiometric
245 resolution and radiometrically calibrated as described in Zarco-Tejada et al. (2013c). The
246 hyperspectral sensor flown on board a manned platform yielding a 6.4 nm full-width at half-
247 maximum (FWHM) with a 25-micron slit in the 400–885 nm region and 60 cm pixel size
248 (Fig. 1). Data acquisition and storage module achieved a 50 fps (frames per second) with 18-
249 ms integration time. The 8-mm optical focal length lens yielded an instantaneous field of
250 view (IFOV) of 0.93 mrad and an angular field of view (FOV) of 49.82°. Radiance values
251 were converted to reflectance using total incoming irradiance measured at the time of image
252 acquisition. Field measurements were taken with an ASD Field Spectrometer (FieldSpec
253 Handheld Pro, ASD Inc, CO, USA) with a cosine corrector-diffuser probe for the 350-1050
254 nm spectral range at lower resolution (3 nm FWHM). The ASD Field Spectrometer was first
255 calibrated using a Spectralon (SRT-99-180, Labsphere, NH, USA) white panel. ASD
256 measurements were resampled to 6.5 nm by Gaussian convolution to match the irradiance

257 spectra to the spectral resolution of the radiance imagery acquired by the hyperspectral
258 airborne sensor.

259 The high resolution hyperspectral imagery (Fig. 1a) acquired over the oak forest (Fig. 1b)
260 enabled the identification of different scene components (Fig. 1c) for field validation
261 purposes. The fluorescence signal was quantified using the 760-nm O₂-A in-filling method
262 based on the Fraunhofer line depth (FLD) calculated from a total of three bands (FLD3):

263

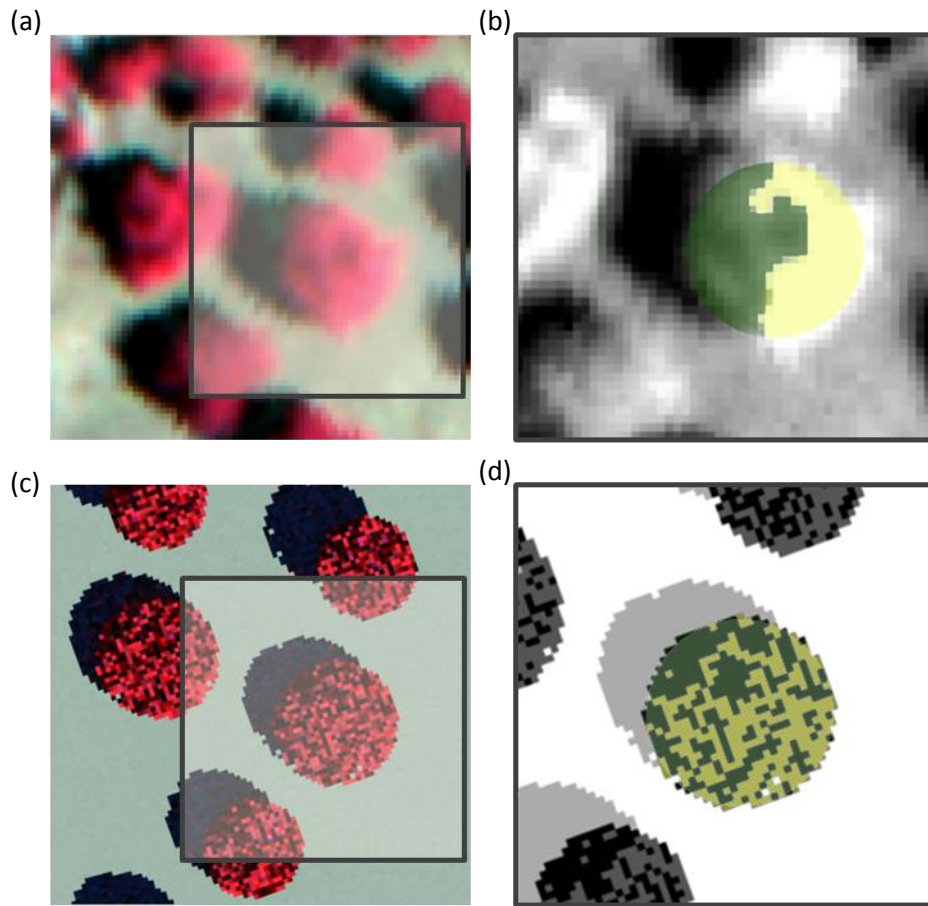
$$264 \quad F = \frac{E_{out} * L_{in} - E_{in} L_{out}}{E_{out} - E_{in}} \quad (1)$$

265

266 where radiance, L, corresponds to L_{in} (L761), L_{out} (average of L747 and L780 bands), and the
267 irradiance, E, to E_{in} (E761), and E_{out} (average of E747 and E780 bands).

268 Other vegetation indices mostly related with physiology such as the Photochemical
269 Reflectance Index (PRI) (Gamon et al., 1992) and the Red Edge ratio index (RE) (Zarco-
270 Tejada et al., 2001) and with canopy structure such as the NDVI (Rouse et al., 1972) were
271 also tested in this study.

272 The hyperspectral imagery acquired enabled full crown pixels identification (Fig. 2a) and
273 shaded and sunlit components within each crown (Fig. 2b). Thus, in order to assess the
274 implications of scene components on the SIF signal when quantified in large pixels, FLD was
275 quantified from three different strategies of aggregation (Fig. 2): from only sunlit pixels
276 within each crown, all pixels from each tree crown (full crown pixels, including shaded and
277 sunlit pixels) and from aggregated pixels at 30x30 m (including tree crown, bare soil and
278 shadows).



279

280 **Fig. 2.** Example of a 30x30 m scene (highlighted squared) of the micro-hyperspectral imagery
 281 acquired at 40 cm resolution in color-infrared (a) and sunlit and shadowed component identification
 282 of the crown on the micro-hyperspectral imagery (b). Example of a 30x30 m scene (highlighted
 283 squared) simulated with FluorFLIGHT (c) and sunlit and shadowed component identification on
 284 simulated images (d).

285

286 **2.3. FluorFLIGHT model**

287 FluorFLIGHT is a 3-D integrated RTM to calculate reflectance and fluorescence in the
 288 observation direction as a function of canopy components. It is based on existing theory of
 289 radiative transfer by coupling the leaf fluorescence model FLUSPECT and the 3-D ray-
 290 tracing model FLIGHT to account for canopy heterogeneity. The FluorFLIGHT model was
 291 specifically developed to assess the sensitivity of the fluorescence signal on heterogeneous
 292 forest canopy images.

293 FLUSPECT model is based on the Kubelka-Munk equation and requires a total of 7 inputs
294 included in Table 2. Six of them are original parameters from the PROSPECT model (Feret et
295 al., 2008; Jacquemoud and Baret, 1990), i.e., leaf structure parameter N , chlorophyll a+b
296 (C_{a+b}) and carotenoid (C_{c+x}) content, water equivalent thickness in cm (C_w), dry matter
297 content (C_m) and the senescence material (C_s). An additional parameter, the fluorescence
298 quantum efficiency (F_i), from 0 (no fluorescence) to 0.1 (10% fluorescence), is required to
299 calculate the excitation-fluorescence matrix for each photosystem (PSI and PSII). For this
300 study, the F_i of PSI was fixed at one-fifth that of PSII, as the total spectrally integrated flux of
301 PSII has been reported to be typically fivefold that of PSI (Franck et al., 2002). The
302 FLUSPECT model generates two excitation-emission fluorescence matrices (EEFM) from
303 640-850 nm at 1 nm resolution and the reflectance and transmittance spectra of a leaf from
304 400-850 nm at 1 nm resolution. The EEFM matrices are separately generated for each
305 photosystem for both sides of the leaf -the illuminated and the shaded side of the leaf-,
306 backward and forward scattering matrices, respectively.

307 The FLIGHT model is based on Monte Carlo and deterministic ray tracing techniques to
308 simulate the observed reflectance response of 3-D vegetation canopies (North, 1996, North et
309 al., 2010). Multiple scattering within crown boundaries and between the crowns and other
310 canopy components is modelled to account for canopy heterogeneity. It has formed one of a
311 set of six benchmark models for RTM evaluation under the RTM Intercomparison (RAMI)
312 project (Widlowski et al., 2008, 2007). Structural data may be specified as a statistical
313 distribution, derived from field measurements or by direct inversion from lidar data (Bye et
314 al., 2017). FLIGHT calculates directional reflectance by accumulating photon energy in the
315 observation direction as a function of different forest canopy components defining the canopy
316 structure (crown shape and size, tree height, position, density and distribution) (Table 2). The

317 distribution and absorption of light intercepting the canopy was calculated with a modified
 318 version of FLIGHT including the EEFM contribution to radiance.

319 **Table 2.**

320 Nominal values and range of variation used in FluorFLIGHT simulation analysis based on field data
 321 measurements.

Variable	Variable code	Nominal values	Range
<i>FLUSPECT</i>			
Mesophyll structure	N	2.1	-
Chlorophyll content	C_{a+b} ($\mu\text{g}/\text{cm}^2$)	35	10-60
Carotenoid content	C_{x+c} ($\mu\text{g}/\text{cm}^2$)	12	5-20
Water content	C_w (mg/cm^2)	0.013	-
Dry matter	C_{dm} (mg/cm^2)	0.024	-
Senescent material	C_s	0	0
Fluorescence quantum efficiency	F_i	0.04	0-0.1
<i>FLIGHT</i>			
Solar zenith, view zenith ($^\circ$)	θ_s, θ_v	31.3, 0.0	-
Solar azimuth, view azimuth ($^\circ$)	Φ_s, Φ_v	30.44, 0.0	-
Total LAI		3.15	0-3
Leaf angle distribution	LAD[1-9]	0.015, 0.045, 0.074, 0.1, 0.123, 0.143, 0.158, 0.168, 0.174	
Fractional cover (%)	FC	70	0-100
Crowns shape	CSh	ellipsoid	
Crown coordinates, radius, and centre to top distance	X_i, Y_i, E_{xy}, E_z (m)	6.0, 5.0	
Minimum and Maximum height to first branch (m)	Hmin, Hmax	4.0, 10.0	
Density (trees/ha)	D	60	8-400
Soil reflectance	$\rho_{\lambda\text{soil}}$	ASD measurements	
Soil roughness	Θ_{soil}	0	
Solar irradiance	$\rho_{\lambda s}$	ASD measurements	

322

323 In addition, the canopy model requires a soil spectrum, solar irradiance (inputs from Table 2)
 324 and the six outputs obtained from the leaf model: leaf reflectance without fluorescence (ρ_n),
 325 leaf transmittance without fluorescence (τ_n), and the backward and forward fluorescence
 326 matrices for each photosystem (MbI, MbII, MfI, MfII).

327 Within FLIGHT, illumination at a facet such as a leaf is calculated as the sum of direct and
 328 diffuse incoming light. For a facet L with normal vector Ω_L , viewed from vector direction Ω_m
 329 and illuminated from vector direction Ω_0 , the surface-leaving radiance contribution to the
 330 detector excluding fluorescence is defined according to the equation:

331

$$332 \quad I_L(\lambda) = I_0(\lambda)\gamma_L(\Omega_0 \rightarrow \Omega)P_0 + \frac{1}{m} \sum_1^m I_m(\lambda)(\Omega_m)\gamma_L(\Omega_m \rightarrow \Omega) \quad (2)$$

333

334 Where I_0 is the direct solar beam illumination radiance at wavelength λ , and I_m denotes a
 335 sample of the incoming diffuse field from direction Ω_m , and γ_L is the bi-directional
 336 reflectance or transmittance factor for facet L . P_0 has value 1 if there is a direct path to the
 337 source illumination, and 0 otherwise.

338 The non-fluorescent scattering contribution for an individual facet L at wavelength λ is
 339 approximated here using a bi-Lambertian reflectance/transmittance model:

340

$$341 \quad \gamma_L(\Omega_L, \Omega' \rightarrow \Omega) = \begin{cases} \pi^{-1} \rho_n(\lambda) |\Omega \cdot \Omega_L|, & \text{if } (\Omega \cdot \Omega_L)(\Omega' \cdot \Omega_L) < 0 \\ \pi^{-1} \tau_n(\lambda) |\Omega \cdot \Omega_L|, & \text{if } (\Omega \cdot \Omega_L)(\Omega' \cdot \Omega_L) > 0 \end{cases} \quad (3)$$

342 The fluorescence contribution F_L is calculated using similar equations, but using the full
 343 fluorescent scattering matrices at leaf level, sampling direct and diffuse leaf-level incident
 344 illumination within the excitation range 400-750 nm:

345

$$\begin{aligned}
& F_L(\lambda) \\
346 \quad & = \sum_{k=400}^{750} \left(I_0(k) \gamma_F(\Omega_0 \rightarrow \Omega) P_0 + \frac{1}{m} \sum_1^m I_m(k) (\Omega_m) \gamma_F(\Omega_m \rightarrow \Omega) \right) \quad (4)
\end{aligned}$$

347 where

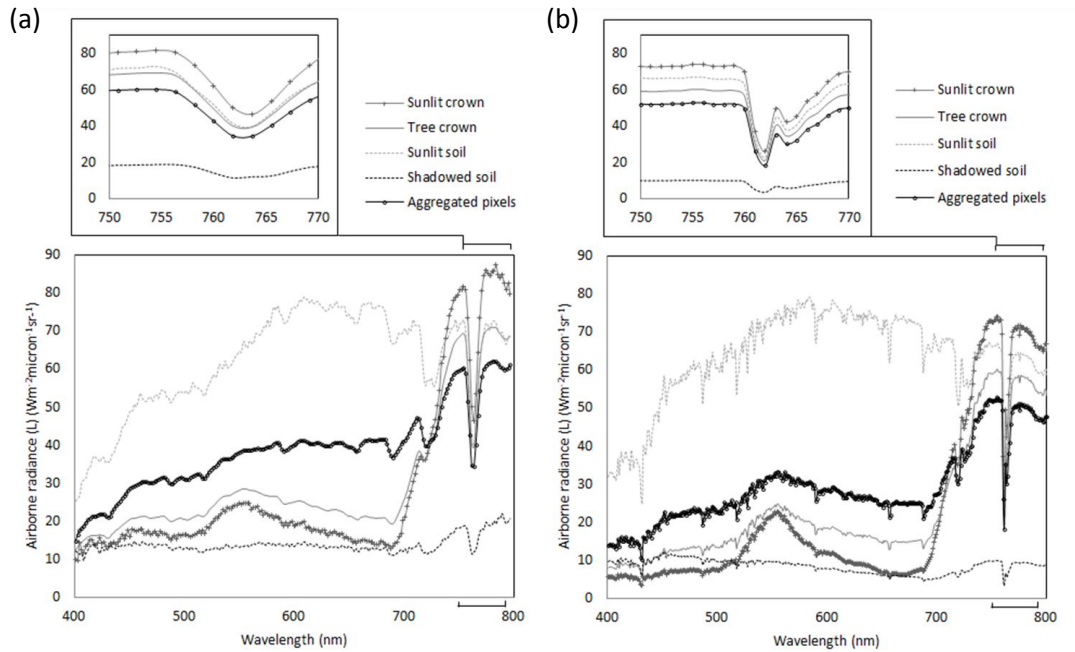
$$\begin{aligned}
& g_F(W_L, W' \rightarrow W) \\
348 \quad & = \begin{cases} \rho^{-1} Mb [k, /] |W \cdot W_L|, & \text{if } (W \cdot W_L) (W' \cdot W_L) < 0 \\ \rho^{-1} Mf [k, /] |W \cdot W_L|, & \text{if } (W \cdot W_L) (W' \cdot W_L) > 0 \end{cases} \quad (5)
\end{aligned}$$

349

350 Where Mb is the sum of backward scattering matrices for PSI and PSII contributions, and Mf
351 for forward scattering. Total measured radiance is calculated as the sum of the reflected light
352 and fluorescent emission terms. The full evaluation of the fluorescence scattering matrices at
353 each photon interaction at leaf level allows inclusion of fluorescent emission in TOC spectra,
354 accounting for 3-D structure, multiple scattering, and leaf-level light environment.
355 Furthermore, the simulated reflectance at the canopy level accounts for crown overlapping,
356 mutual shading, and multiple scattering among crowns. Sunlit and shadowed pixels of the
357 crown are identified based on the scene components mask derived from the FluorFLIGHT
358 model simulations (Fig. 2c, d). This makes it possible to understand the contribution of each
359 component at different resolutions, particularly important for sensors acquiring data with
360 lower spatial resolutions and therefore, with higher aggregation effects (Fig. 3). As an
361 example, the fluorescence peak experimentally observed in canopy reflectance and simulated
362 with FluorFLIGHT can be shown in (Fig. 3a, b).

363 The model is originally developed at 1 nm FWHM. Nevertheless, for comparisons against the
364 airborne hyperspectral imagery, the model simulations are convolved to 6.5 nm FWHM to
365 match the spectral resolution of the radiance imagery acquired by the hyperspectral airborne
366 sensor. If no convolution is carried, the FWHM of the 1 nm (model) vs 6.5 nm (image) would

367 derive different levels of fluorescence emission. Accounting for the bandwidth of the imagery
 368 enables the comparison between the fluorescence retrieved from the model and the one
 369 retrieved from the image at the tree crown level.



370
 371 **Fig. 3.** Example of the spectral radiance extracted from the micro-hyperspectral image (a) and from
 372 FluorFLIGHT simulated radiance (L) (b) for different scene components: sunlit crown, full crown,
 373 sunlit soil, shadowed soil and aggregated pixels (30x30 m) in the O₂-A feature used for fluorescence
 374 quantification. Spectral features extracted from Fig. 2.

375

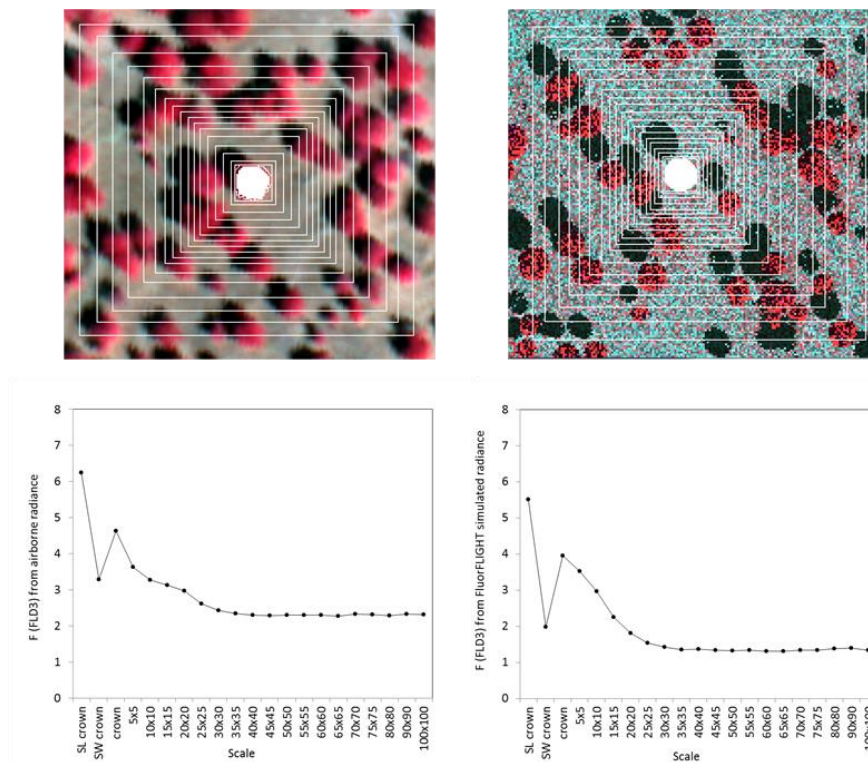
376 2.4. Model simulation approach

377 The coupled 3-D fluorescence model FluorFLIGHT was used in this study with two primary
 378 objectives: i) the analysis of forest structure effects on SIF retrievals at high resolution scale,
 379 ii) the estimation of SIF from coarse-spatial-resolution imagery by Look-Up Table (LUT-
 380 based) model inversion to account for the canopy architecture.

381 *i) Modelling forest canopy structural effects on fluorescence signal.*

382 FluorFLIGHT was used to analyse the variation of SIF as a function of forest structural
 383 components. The aim of this analysis was to assess the influence of scene components on the

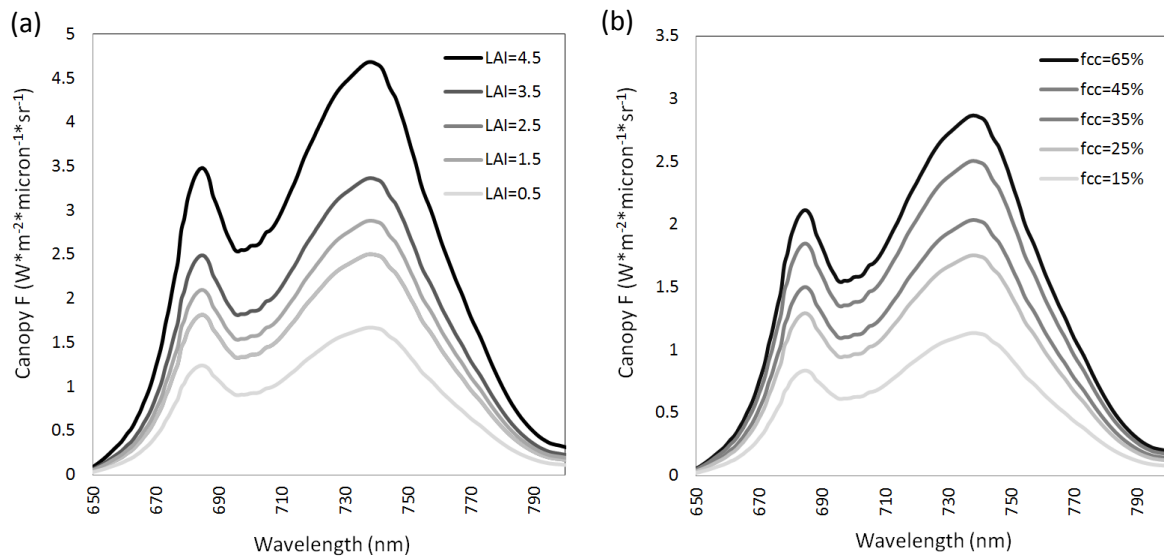
384 retrieval of the chlorophyll fluorescence signal by identifying the key variables determining
 385 SIF variations at different scales. To do this, SIF was quantified using the 760-nm O₂-A in-
 386 filling method (FLD3) from FluorFLIGHT simulated data from three different strategies of
 387 aggregation (Fig. 2): from only sunlit pixels within each crown, all pixels from each tree
 388 crown and from aggregated pixels at 30x30 m (including tree crown, bare soil and shadows).
 389 This selection was based on the SIF variations found over different levels of aggregation in
 390 both, imagery and simulated spectra (Fig. 4). Fig. 4 shows the variation in SIF extracted from
 391 the original high-resolution airborne hyperspectral image (Fig. 4c) and from a FluorFLIGHT
 392 image (Fig. 4d) as a result of increasing the pixel-aggregation level from sunlit crown pixels
 393 to aggregated pixels of 100x100 m window.



394
 395 **Fig. 4.** Subplots emulating the aggregation effects due to the spatial resolution overlaid onto the
 396 micro-hyperspectral imagery acquired at 60 cm resolution (a) and a FluorFLIGHT simulated image
 397 (b), both in colour-infrared. F (FLD3) variation based on the hyperspectral image (c) and the
 398 simulated image (d) estimated from: sunlit pixels of the crown (SL crown), shadowed pixels of the
 399 crown (SW crown), full crown pixels (crown=SL+SW) and eighteen aggregated pixels from a 5x5 m
 400 window to a 100x100 m window.

401

402 FluorFLIGHT simulations were calculated for a set of leaf fluorescence quantum efficiency
 403 (F_i) values and forest structure scenarios. Leaf fluorescence signal was simulated with a
 404 varied range of F_i between 0 and 0.1. To cover the full range of canopy structural scenarios, a
 405 varied range of LAI (0-4), FC (0-100%) and density (10-200 trees/ha) were used to simulate
 406 the spectral response at the crown level (Fig. 5a) and at the aggregated canopy level (Fig. 5b).

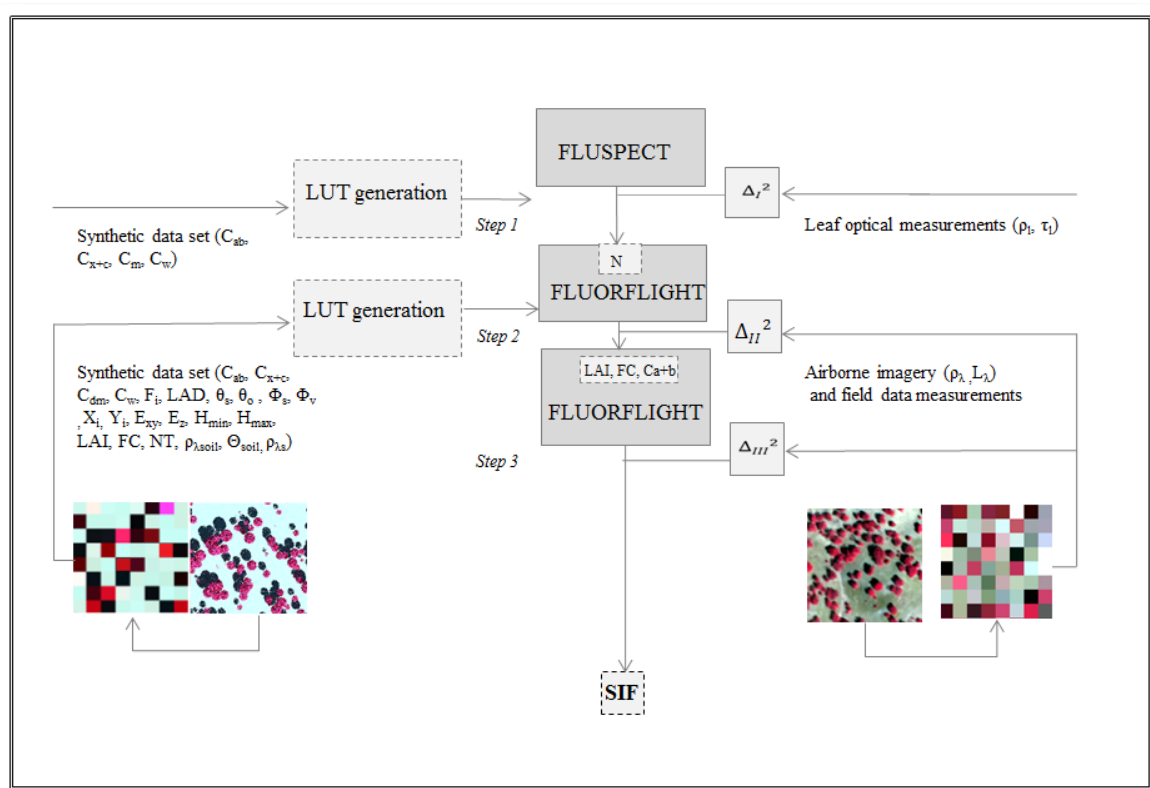


407
 408 **Fig. 5.** Simulated canopy radiance including the effects of fluorescence using the FluorFLIGHT
 409 model for a varied range of leaf area index (LAI) (0.5-4.5) (a) and fractional cover (FC) (15-65%) (b).
 410 Fluorescence quantum yield efficiency at photosystem level ($F_i=0.06$). All other input parameters of
 411 the model were set using nominal values included in Table 1.

412
 413 *ii) Fluorescence retrieval with FluorFLIGHT and hyperspectral data for detecting forest*
 414 *stress.*

415 The potential of using FluorFLIGHT to predict SIF from spatially aggregated pixels in a
 416 heterogeneous oak forest was analyzed. For this purpose, FluorFLIGHT was used in a multi-
 417 step LUT-based inversion scheme (Fig. 6) to retrieve full crown SIF from a complex scene
 418 accounting for the influence of scene structure and composition. The estimation of vegetation
 419 fluorescence emissions was assessed from a spatial aggregation of 30x30 m, which included
 420 variations in crown coverage and shadows and sunlit proportions. The lack of complex RTMs

421 to simulate SIF in heterogeneous canopies (Zarco-Tejada et al., 2013b) has constrained the
 422 progress on the fluorescence interpretation in forest canopies. As shown in Fig. 6, SIF was
 423 quantified by inversion based on the FLD3 estimated from the airborne image using the LUT
 424 derived from FluorFLIGHT. As a prior step, an optimal parameter combination of N, LAI,
 425 C_{a+b} , and FC was iteratively retrieved. Lastly, SIF retrievals were then validated based on
 426 ground measurements of the physiological variables related with the photosynthetic activity
 427 of the vegetation such as DEPS, ψ , and Fs.



428
 429 **Fig. 6.** Overview of the processing steps followed in the retrieval of sun-induced fluorescence (SIF)
 430 showing the input variables used for the simulations. Inputs description included in Table 1.

431
 432 The detailed description of the inversion process shown in Fig. 6 is detailed below.

433 Step 1. N determination by minimizing the merit function (Δ_f):

434

435
$$\Delta_I^2 = \sum_n [(\rho_m(\lambda_i) - \rho^*(\lambda_i, N))^2 + (\tau_m(\lambda_i) - \tau^*(\lambda_i, N))^2] \quad (6)$$

436

437 Where $\rho_m(\lambda_i)$, $\tau_m(\lambda_i)$ are the leaf reflectance and transmittance at wavelength λ measured
 438 from the field, and ρ^* and τ^* denote the modelled ones. A synthetic spectra database was
 439 simulated with FLUSPECT producing 1000 simulations with a set of N random values (1-4).
 440 Input parameters were set up to simulate the typical range of variation observed in the field
 441 Table 2.

442 Step 2. Green FC determination by minimizing the merit function (Δ_{II}):

443 For this purpose, FluorFLIGHT was used for retrieving an optimal set of vegetation
 444 parameters (FC, LAI and C_{a+b}) using a LUT-based inversion scheme using aggregated pixels
 445 of 30x30 m.

446

447
$$\Delta_{II}^2 = \sum_n [vi_m - vi^*(\Theta)]^2 \quad (7)$$

448

449 Where vi_m is the vegetation index used for the retrieval of each parameter calculated from
 450 measured canopy reflectance and $vi^*(\Theta)$ and from modelled canopy reflectance for a given
 451 set of input parameters Θ . FC and LAI were retrieved using the NDVI (Rouse et al., 1974);
 452 mean values of the range of possible solutions within the LUT were used since there is
 453 ambiguity between FC and LAI corresponding to a given VI value without additional
 454 constraints on allowable structure. C_{a+b} was retrieved using the RE (Zarco-Tejada et al., 2001)
 455 that showed robustness to shadow and structural effects in forest canopies. A synthetic
 456 spectra database was simulated with FluorFLIGHT producing 1000 simulations. Leaf input

457 parameters were set up to simulate the typical range of variation observed in the field
 458 ($C_{a+b}=10-80 \mu\text{g}/\text{cm}^2$; $C_{x+c}=2-18 \mu\text{g}/\text{cm}^2$; $C_w=0.02$; $C_{dm}=0.01$). Leaf level spectra were
 459 simulated using $N=2.1$ as derived from inversions of leaf-level optical measurements of field
 460 samples estimated above (Step 1). Leaf fluorescence signal was simulated with a varied range
 461 of F_i ranging between 0 and 0.1. The nominal inputs used at the leaf level are shown in Table
 462 2.

463 At the canopy level, forest structure attributes such as tree height, crown diameter and LAI
 464 were randomly varied for different oak-forest cover structures to generate a range of FC
 465 between (0-100%). Table 2 shows the input parameters required by the model and the
 466 nominal variation range for the parameters used for canopy modelling with FluorFLIGHT.
 467 The spectral sampling of the simulations was initially adjusted to 1 nm covering a range for
 468 400 to 1050 nm. Then, simulated images were resampled to the spectral bandwidth of the
 469 hyperspectral airborne sensor through Gaussian convolution. The inverted values of FC, LAI
 470 and C_{a+b} were obtained by matching measured and modelled LUT vi through (7) and finding
 471 the optimal parameter combination (Leonenko et al., 2013; Prieto-Blanco et al., 2009) and
 472 validated against FC, LAI and C_{a+b} field measurements.

473 Step 3. Fluorescence inversion using the inverted FC, LAI and C_{a+b} as multi-constraint
 474 regularization.

475 The simulated spectra with FluorFLIGHT were used here to retrieve SIF using the inverted
 476 values of FC, LAI and C_{a+b} (Step 2) as constraints in a regularization strategy attending to
 477 reduce the influence of structural canopy variables of the fluorescence signal.

478

479
$$\Delta_{III}^2 = \sum_n [F_m(FLD3) - F^*(FLD3, \theta)]^2 \quad (8)$$

480

481 Where $F_m(FLD3)$, is the FLD3 calculated from measured canopy radiance and $F^*(FLD3, \Theta)$
482 is the FLD3 calculated from modelled canopy reflectance for a given set of input
483 parameters Θ . In both cases, radiance spectra were extracted from 30x30 m aggregated pixels
484 (Fig. 6). The inverted values of crown FLD3 and leaf F_i were obtained by matching measured
485 and modelled LUT spectra through (8) and finding the optimal values.

486 Finally, model-based retrievals derived from hyperspectral imagery were compared to
487 ground-truth fluorescence data. Additionally, results were also compared to other
488 physiological variables collected on the ground.

489

490 **3. Results.**

491 *3.1. Relationships between physiological variables and airborne F (FLD3).*

492 The capability of F (FLD) of discriminating different functional status of the vegetation was
493 analysed and compared to other vegetation spectral indices (Table 3). The relationships
494 between F (FLD3) quantified from full crown vegetation pixels and different physiological
495 variables (F_s , DEPS, and ψ) were statistically significant ($p < 0.01$) and stronger than the
496 relationship with other physiological vegetation indices such as PRI or RE. The weakness
497 relationship found was between the physiological variables and the NDVI, a sensitive
498 indicator of canopy structure.

499 The high spatial resolution obtained by the hyperspectral imagery (60 cm resolution) enabled
500 the identification of each scene components (Fig. 2), enabling the estimation of F (FLD3)
501 from sunlit crowns pixels. The sunlit-crown F (FLD3) extracted was compared against
502 (F_s , ψ and DEPS) measured at the tree-level, yielding ($r^2 = 0.63$; $p < 0.001$) (Fig. 7a) between

503 sunlit-crown F (FLD3) and ground measured DEPS. Slightly lower relationships were found
 504 by comparing F (FLD3) and ψ ($r^2= 0.57$; $p<0.01$) (Fig. 7b). Statistically significant
 505 relationships between sunlit-crown F (FLD3) and DEPS and ψ were consistent with the
 506 relationships obtained between leaf F_s and airborne F (FLD3) ($r^2= 0.74$; $p<0.001$) (Fig. 7c).
 507 These results indicate that SIF retrieved from sunlit vegetation radiance of the crowns was a
 508 good indicator of physiological status of the trees within the context of this study.

509 **Table 3.**

510 Correlation coefficient R between steady-state fluorescence yield (F_s), de-epoxidation state of the
 511 xanthophyll cycle (DEPS) and water potential (ψ) and crown-based spectral vegetation indices,
 512 including structural and physiological vegetation indices.

Functional-related indices		F_s		DEPS		ψ	
		R	R2	R	R2	R	R2
Fluorescence	FLD3	0.79	0.62***	-0.67	0.44**	0.71	0.5**
Photochemical reflectance index	PRI	-0.45	0.2	0.65	0.42**	-0.51	0.27*
Chlorophyll -RE	R750/R710	-0.24	0.06	0.13	0.02	-0.22	0.04
Structure-NDVI	NDVI	-0.16	0.02	0.16	0.03	-0.18	0.03
	<i>Non-significant</i>	P>0.05					
	<i>Significant**</i>	P<0.01					
	<i>Highly significant**</i>	P<0.001					

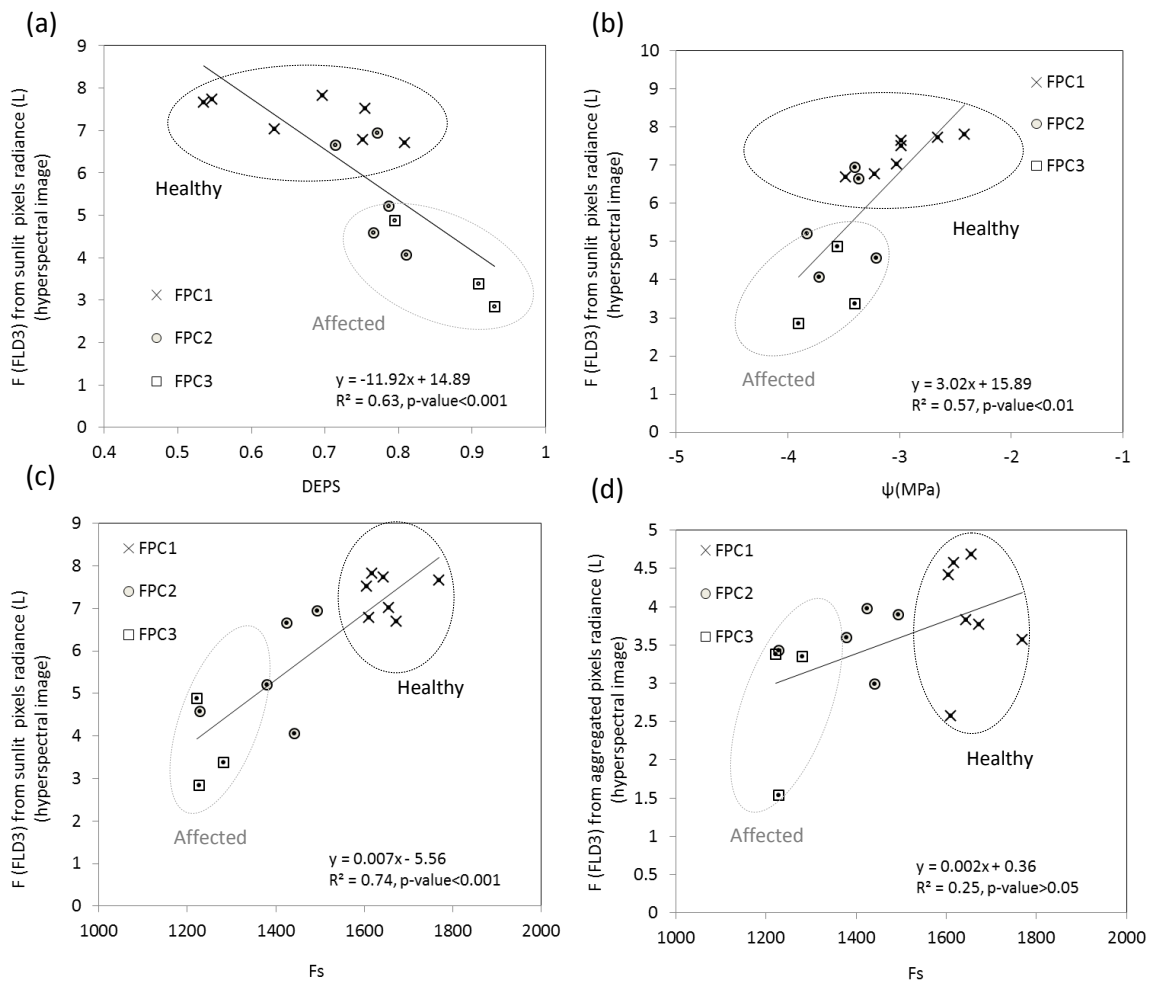
513

514 It was also observed that healthy trees (FPC1) showed higher F_s and ψ and lower DEPS while
 515 affected trees (FPC3) showed the opposite, with moderate level of affectation (FPC2) in
 516 between. These results showed that sunlit-crown F (FLD3) was also sensitive to the stress
 517 levels, tracking the physiological change forced by forest decline processes.

518 Additionally, the F (FLD3) was calculated from spectra extracted from aggregated pixels
 519 from a 30x30 m window using as central point the location of each tree. The SIF signal
 520 retrieved from aggregated pixels was lower than that extracted from sunlit crown pixels with
 521 F (FLD3) values ranged between (1.9-4.9 and 2.5-8) $Wm^{-2}\mu m^{-1}sr^{-1}$ respectively (Fig. 7c, d).
 522 As it is shown in Fig. 7d, the sensitivity to F_s ground-data was lower with F (FLD3) retrieved
 523 from aggregated radiance pixels, yielding a ($r^2= 0.25$; statistically non-significant). These

524 results demonstrates the expected effect caused by the canopy architecture on SIF retrieved
 525 from mixed pixels, and therefore, the need of modelling those effects while using coarse-
 526 spatial resolution images.

527



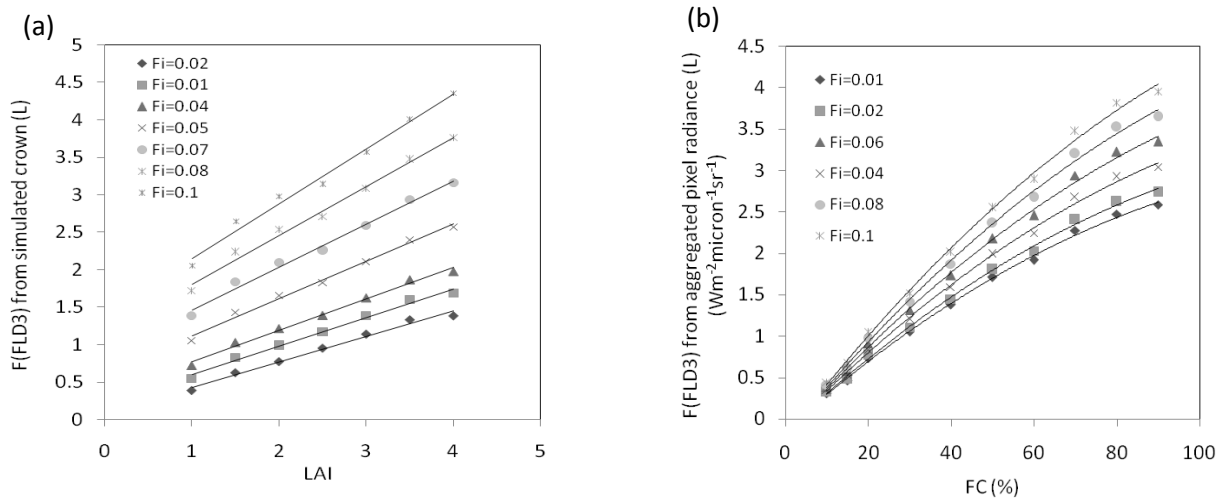
528

529 **Fig. 7.** Relationship between de-epoxidation state of the xanthophyll cycle (DEPS) (a) and water
 530 potential (b) against F (FLD3) from sunlit pixel radiance L retrieved from the hyperspectral image.
 531 Relationships between steady-state fluorescence yield (F_s) ground-data measurements of 15 oak
 532 trees and airborne-based F (FLD3) retrieved from sunlit pixel radiance (c) and 30x30 m aggregated
 533 pixels radiance (L) retrieved from the hyperspectral image (d). Trees with higher and lower level of
 534 affection are highlighted within a dashed grey and black line respectively.

535

536 *3.2. Modelling forest structural effects on SIF at the canopy level.*

537 The sensitivity of the fluorescence signal to the variation in canopy structural components
 538 based on the relationships between crown SIF and SIF from 30x30 m aggregated pixels is
 539 presented in Fig. 8. F (FLD3) was retrieved for a range of LAI, tree density and percentage of
 540 FC values showing the influence of scene components on fluorescence signal from full
 541 crowns (Fig. 8a) and aggregated pixels (Fig. 8b).



542 **Fig. 8.** Effects of forest structural variables on simulated canopy fluorescence (FLD3) as a function of
 543 LAI (0-5) at the crown level (a) and fractional cover FC (10-90%) at the canopy level (b). All other
 544 input parameters of the model were set using nominal values included in Table 1.

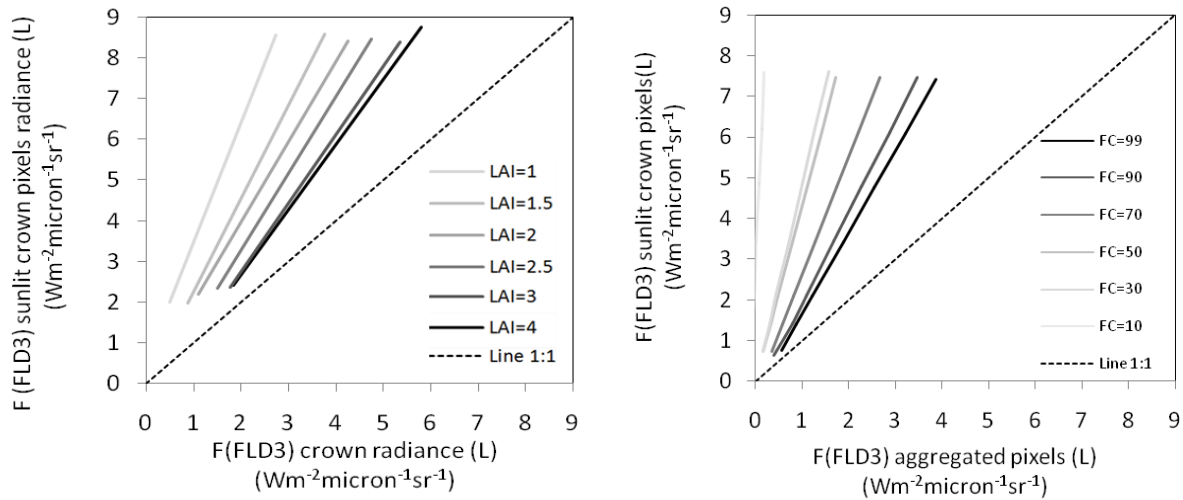
545

546 The sensitivity of SIF to variations in forest canopy structure is higher at lower values of LAI
 547 and FC, especially with aggregated pixels (Fig. 8b). According to these results, SIF signal
 548 variations at the crown and canopy level can only be directly linked to variations in
 549 photosynthetic activity when structural parameters remain constant (Fig. 8). Only in this case,
 550 F (FLD3) increased as the F_i input parameters increased.

551 Additionally, FluorFLIGHT simulations were used to develop relationships between sunlit
 552 crown pixels, crown pixels and aggregated pixels as a function of FC and LAI. As shown in
 553 Fig. 9, LAI and FC were varied to generate a range between 1-4 and 10-100%, respectively.

(a)

(b)



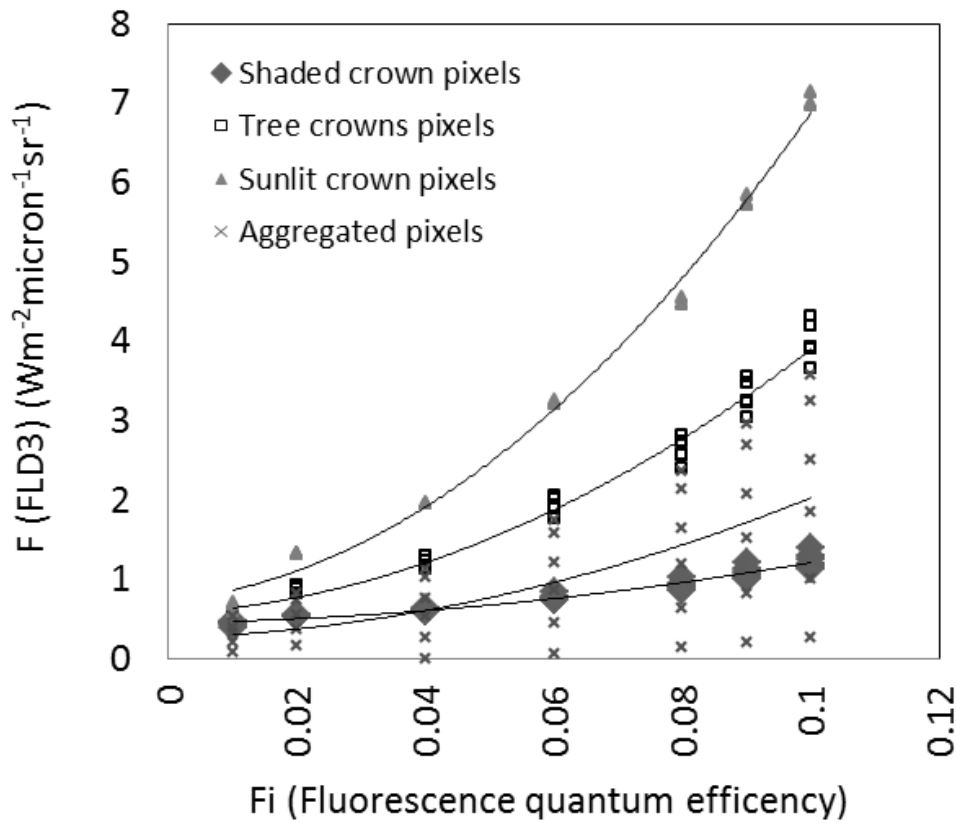
555 **Fig. 9.** Relationships between FluorFLIGHT simulations of canopy L obtained from sunlit crown
 556 pixels and full crowns as a function of LAI (1-4) (a). Relationships between FluorFLIGHT
 557 simulations of crown L obtained from sunlit crowns and aggregated pixels as a function of FC (10-
 558 90%) (b).

559

560 The simulated SIF was calculated using the FLD method for the spectral radiance extracted
 561 from sunlit crowns and then compared to different components of the scene such as full
 562 crown (Fig. 9a) and aggregated pixels of the scene (Fig. 9b). Modelling results show that the
 563 SIF signal retrieved from exposed crown and full crown pixels is higher than for aggregated
 564 pixels. The differences are even significant between the SIF signal retrieved from sunlit
 565 pixels and full crown pixels (Fig. 9a) with slightly higher values for exposed crowns. The
 566 results of quantifying SIF from 30x30 m aggregated pixels as a function of LAI (Fig.9a) and
 567 FC (Fig. 9b) show the large effects of both parameters of the fluorescence quantification. The
 568 contribution of a small percentage of sparse grass component on the soil reflectance
 569 measured from ground measurements hindered F (FLD3) to reach values slightly above zero.

570 Additionally, (Fig. 10) shows the impact on SIF retrieval through the FLD3 method when it
 571 is retrieved from different levels of aggregation (sunlit crown pixels, full crown pixels and
 572 aggregated pixels) for a varied range of F_i , LAI and FC. Comparing the results obtained for

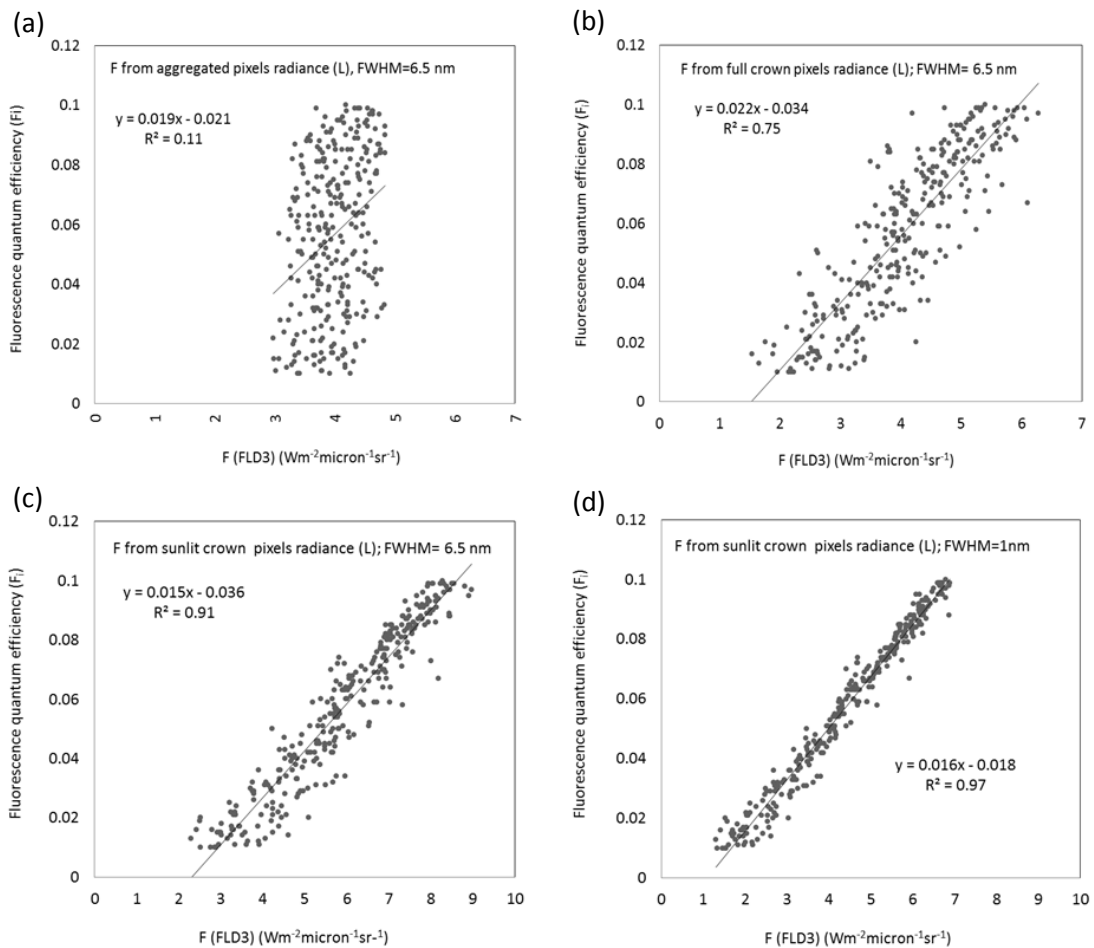
573 the different levels of aggregation, changes in aggregated pixels caused highest uncertainties
 574 in retrieved F (FLD3), followed by full crown pixels and shaded pixels. In contrast, LAI
 575 variations exerted a small variation in F (FLD3) retrieved from sunlit pixels. The SIF signal
 576 retrieved from sunlit crowns ranged between 0 and 8 $\text{Wm}^{-2}\mu\text{m}^{-1}\text{sr}^{-1}$, decreasing the maximum
 577 range with the level of aggregation to 5.2, 3.6 and 1 $\text{Wm}^{-2}\mu\text{m}^{-1}\text{sr}^{-1}$ for full crown, aggregated
 578 pixels and shaded crowns, respectively. Moreover, the SIF signal retrieved from aggregated
 579 pixels was less sensitive to F_i variation than the SIF signal retrieved from sunlit pixels. SIF
 580 signal in shaded crown pixels had minimal sensitivity to F_i variations.



581
 582 **Fig. 10.** Comparison of FluorFLIGHT model-based fluorescence quantum efficiency (F_i) and F
 583 (FLD3) retrieved from shaded and sunlit crown pixels, full crown pixels and aggregated pixels as a
 584 function of LAI (0-4) and FC (0-100%).

585
 586 FluorFLIGHT model simulations obtained using a random synthetic data set of values within
 587 the typical range of variation observed in the field (Table 2) are shown in Fig. 11. F (FLD3)

588 calculated from aggregated radiance pixels was weakly related to F_i due to the large
 589 variability in FC percentages and LAI within simulations (Fig. 11a). A cross-comparison of
 590 simulation results generated from different levels of aggregation shows that the retrieval of
 591 fluorescence improved using fluorescence radiance data from full crown pixels ($r^2=0.75$;
 592 $p<0.001$) and improving even more when sunlit crown pixels were used to calculate SIF
 593 ($r^2=0.91$; $p<0.001$) (Fig. 11b, c). This result was caused by the increase of the effects of
 594 vegetation structure and percentages of soil and shadows in aggregated pixels. The SIF signal
 595 retrieved from sunlit crown pixels is less affected by such effects, increasing its sensitivity to
 596 leaf fluorescence quantum efficiency.



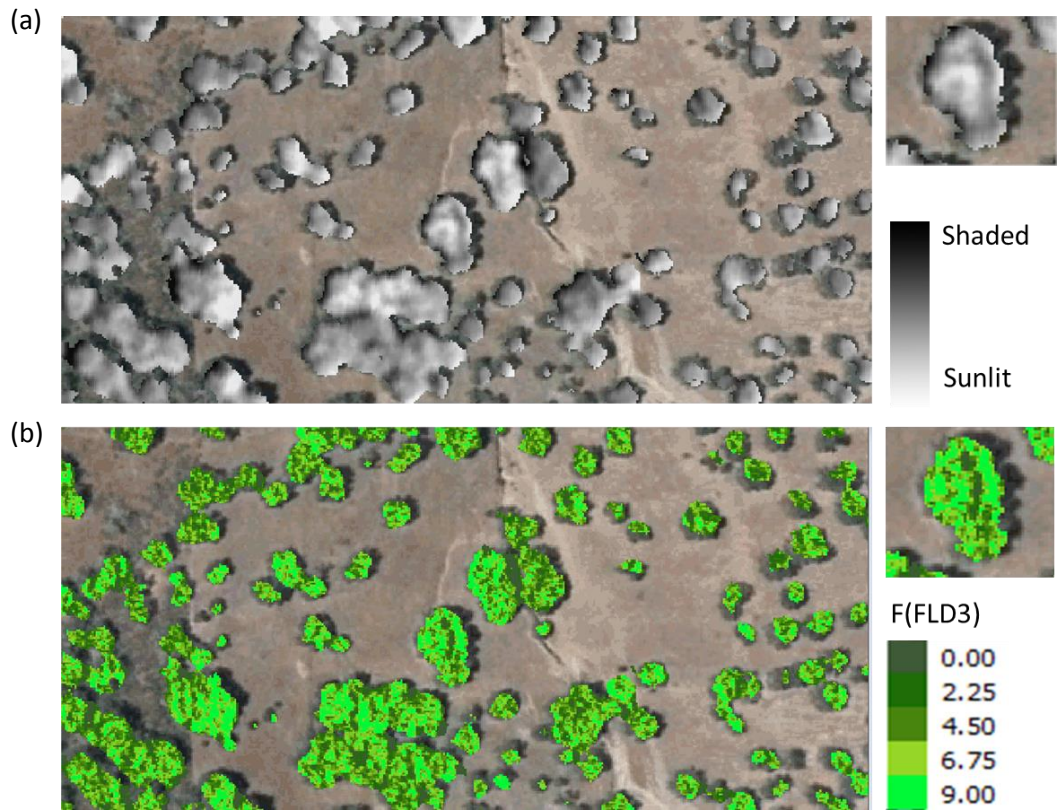
597

598 **Fig 11.** Relationships between the simulated FluorFLIGHT fluorescence quantum efficiency retrieved
 599 (FLD3 method) from synthetic spectra retrieved from 30x30 m aggregated pixels (a), full crown
 600 pixels (b) and sunlit crown pixels at 6.5 nm (c) and at 1 nm (d). LAI (0-4) and FC (40-60%). All other
 601 input parameters of the model were set using nominal values included in Table 1.

602 The sensitivity of SIF signal retrieved from sunlit crowns was further analysed to determine
 603 the impact of using FWHM spectral resolution lower than 1 nm. FluorFLIGHT simulations in
 604 Fig. 11c, d show the results of estimating SIF signal with FLD3 in-filling method against the
 605 fluorescence simulated at 1 nm resolution and 6.5 nm resolution (as a proxy of the spectral
 606 resolution of the micro-hyperspectral imager used in this study). SIF signal retrieved at 6.5
 607 nm and 1 nm had relatively similar accuracies, yielding $r^2=0.90$ (for 6.5 nm data) and $r^2=0.97$
 608 (for 1 nm data).

609 Therefore, the forest structure and composition were shown to play the major role in retrieved
 610 SIF due to the confounding effects caused on aggregated pixels, with much less effect caused
 611 by the spectral bandwidth.

612

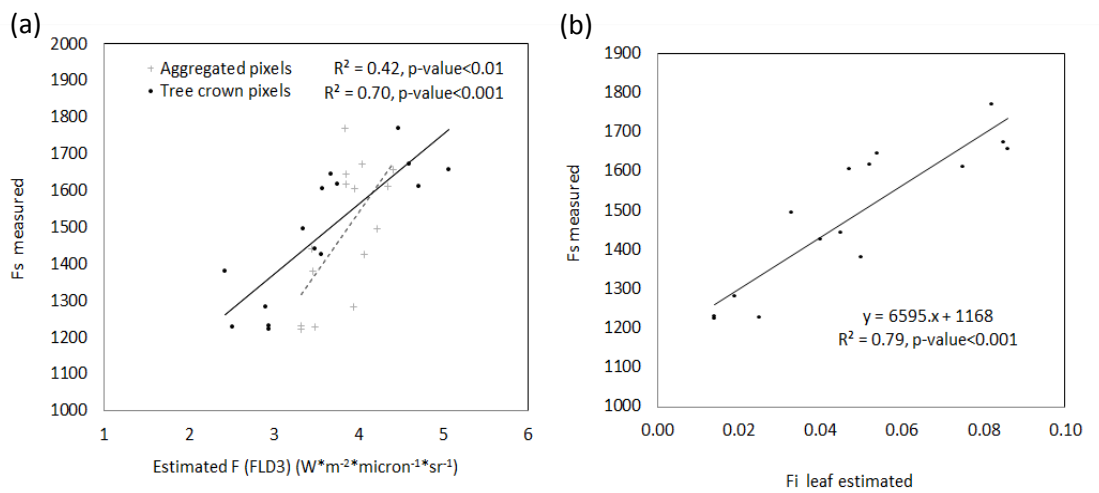


613

614 **Fig. 12.** (a) Sunlit and shadowed component identification of the crown on the micro-hyperspectral
 615 imagery. (b) SIF map showing different values between sunlit and shadowed crown F (FLD3).

616 These modelling results demonstrate the difficulties of interpreting SIF from coarse
 617 resolution images where each aggregated pixel includes a large variety of percentages of
 618 sunlit and shaded vegetation and soil. The effect of the illumination condition of the crowns
 619 corroborates the need to separate the two crown factions as is shown with high resolution SIF
 620 maps (Fig 12).

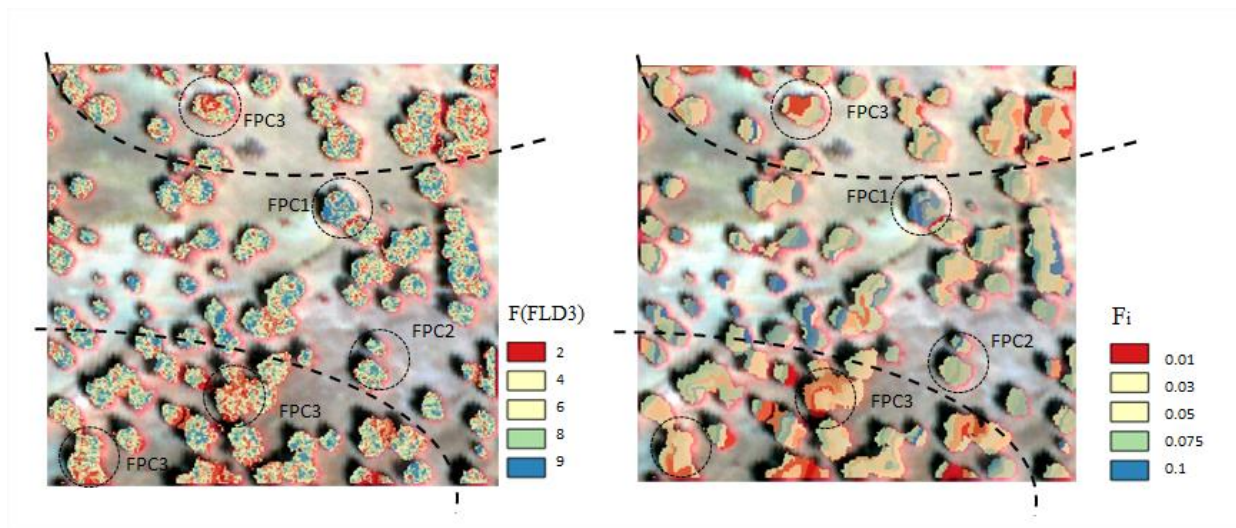
621 Accounting for variations in those percentages, FluorFLIGHT was then used to retrieve SIF
 622 from 30x30m aggregated pixels. The estimation of leaf F_i and crown F (FLD3) through
 623 FluorFLIGHT model inversion is shown in (Fig. 13).



624
 625 **Fig. 13.** Relationships between F_s ground-data measurements and fluorescence estimations retrievals
 626 using FluorFLIGHT applied to aggregated pixels without accounting for pixel aggregation (30x30 m
 627 aggregated pixels) and accounting for pixel aggregation (full crown pixels) with FluorFLIGHT (a)
 628 Leaf level relationship between F_s ground-data measurements and fluorescence quantum yield
 629 estimated with FluorFLIGHT (b).

630
 631 Fig 13a shows the relationship between F_s ground-data and the SIF signal retrieved by
 632 inversion using FluorFLIGHT through the FLD3 method from aggregated pixels (30x30 m).
 633 According to these results, pixel aggregation affected the accuracy in SIF retrieval ($r^2=0.42$)
 634 when pixel aggregation was not considered. The retrieval accuracy was significantly
 635 improved when accounting for the effects of scene components and FC ($r^2=0.70$). When the
 636 F_i was retrieved from FluorFLIGHT accounting for the percentage cover within each pixel,

637 the relationship with F_s ground-data measurements were significantly related ($r^2=0.79$, Fig.
 638 13b). These results are consistent with the relationship found between F_i and the airborne-
 639 based F (FLD3) retrieved from aggregated pixels and sunlit pixels (Fig 11a, c). Fig.14 shows
 640 the output maps after the inversion approach applied at the crown level. The map shows the
 641 spatial variability of fluorescence estimates within the oak forest based on the F (FLD3) and
 642 the F_i inverted from FluorFLIGHT (Fig. 14). The spatial distribution of fluorescence agrees
 643 with the spatial pattern of *Phytophthora* infections showing different susceptibility levels
 644 from trees nearby.



645
 646 **Fig. 14.** F_i retrieval at the crown level estimated from the 60-cm hyperspectral image using the
 647 fluorescence in-filling method F (FLD3) within the oak forest.

648

649 4. Discussion.

650 The consistent relationship between the fluorescence signal SIF retrieved from imagery and
 651 physiological variables (see Fig. 7) supports the hypothesis that SIF signal is a good indicator
 652 of the physiological status of the trees. Although similar observations have been made within
 653 other species e.g., for coastal shrubs (Naumann et al., 2008); for vineyards and orange trees
 654 (Zarco-Tejada et al., 2013a and Zarco-Tejada et al., 2016), this is the first attempt showing a

655 consistent relationship between SIF calculated using the FLD3 method from image pixels and
656 physiological variables such as DEPS, F_s or Ψ across different functional forest health
657 conditions (FPC 1, 2 and 3). In this particular case, SIF was demonstrated to be a good
658 indicator of the susceptibility of oak species to damage associated with root pathogen on
659 water relations. Other physiological vegetation indices such as PRI should be also further
660 explored and potentially applied in combination with SIF. Stress-induced damage in oaks is
661 related with an increase in Ψ (absolute values), an increase in the deposition of xanthophylls
662 and a decline in the chlorophyll fluorescence emission (Fig. 7). These results are promising
663 because the early detection of the decline in the physiological condition of the trees is
664 essential to successfully control and manage threatened forests.

665 A major benefit of using a 60-cm hyperspectral image is that it enables identification of the
666 fluorescence signal emitted by the different components of the canopy. When comparing the
667 relationship between the ground-based F_s against the SIF extracted from sunlit crown and
668 30x30 m aggregated image pixels ($r^2= 0.74$ and $r^2= 0.25$, respectively), we observe a
669 significant decrease in the coefficient of determination when using coarse pixel radiance. The
670 slope of the SIF extracted from sunlit crowns is greater than for 30x30 m aggregated pixels,
671 showing therefore a greater rate of change, probably increased by the reduced effects of the
672 background in vegetation sunlit pixels. The sensitivity of remotely measured SIF to pixel
673 aggregations is mainly produced by the natural variations in canopy structure and chlorophyll
674 concentration of a heterogeneous canopy (Verrelst et al., 2016; Zarco-Tejada et al., 2013b).
675 The variation in SIF showed changes as a function of the pixel aggregation level with the
676 highest value yielded with aggregated pixels from the sunlit part of the crown. SIF retrieved
677 from aggregated resolutions with a higher percentage of shadows (SW crown) and soil
678 yielded lower values. Beyond a spatial resolution of 25x25 m, where the number of soil
679 pixels is twice as large as the crown, the aggregation level no longer exerted any influence on

680 F (FLD3). F (FLD3) derived from simulated data and from the hyperspectral image show
681 similar effects: the highest F (FLD3) values corresponded to sunlit crown pixels, and were
682 approximately 25% higher than F (FLD3) extracted from full crown pixels (simulated
683 images) and 32% higher (hyperspectral images). Shaded crowns dramatically reduced the
684 simulated fluorescence, being 66% lower than F (FLD3) values from sunlit crowns. Shaded
685 crowns had a large effect on the radiance signal derived from hyperspectral images by
686 reducing up to 47% the F (FLD3) values as compared to the sunlit part of the crown. Both,
687 FluorFLIGHT-based F (FLD3) and hyperspectral image-based F (FLD3) were significantly
688 reduced with the increase in pixel aggregation level. These results demonstrate the difficulty
689 of quantifying the fluorescence signal using aggregated pixels beyond the crown scale in
690 heterogeneous canopies.

691 Zarco-Tejada et al., (2013b) investigated the possibility of estimating full crown fluorescence
692 from aggregated pixels. Such efforts addressed the effect of canopy structure of the SIF
693 signal, raising important questions about the need to develop new models to simulate SIF
694 from heterogeneous canopies. The main limitation of their study was the use of the coupled
695 FluorMODleaf + FluorSAIL accounting for the geometry through FLIM, which did not take
696 into account scene components such as crown overlapping or illumination conditions within
697 the canopy in the simulations. The FluorFLIGHT model used in this study is a 3-D RTM that
698 allowed the study of the effects caused by the canopy structure, including sunlit and shaded
699 proportions of the crowns and background effects on the retrieval of fluorescence signal from
700 mixed pixels. The experimental and modelling results demonstrated that the estimation of SIF
701 from sunlit crown pixel radiance is a critical issue affecting the estimation accuracy as the
702 mixture with shaded and background pixels increases.

703 In order to provide a proper interpretation of SIF signal retrieved at global scales it is crucial
704 to decouple the fluorescence signal produced by the photosynthetic activity and the

705 confounding effects produced by the canopy structure and multiple scattering (Damm et al.,
706 2014; Verrelst et al., 2015). The FluorFLIGHT simulation analysis presented here suggests
707 that the canopy structure and composition may affect significantly the quantification of SIF
708 from coarse resolutions at global scale. These results confirm some recent efforts done by
709 other authors in order to provide insights into the key variables that drive SIF from vegetation
710 canopies using RTM approaches within the SCOPE model (Verrelst et al., 2016). However,
711 multiple scattering effects within the canopy cannot be addressed with the 1-D RTM SCOPE.
712 Additionally, FluorFLIGHT used here also investigated the effect of scene components such
713 as the percentage of vegetation or the illumination condition on the interpretation of
714 fluorescence signal retrieved from forest heterogeneous canopies. The proportion of sunlit
715 green vegetation absorbs more light and hence produce a higher SIF intensity (Genty et al.,
716 1989) which explains the higher values in SIF retrieval on sunlit crowns using the FLD3
717 method. These results were demonstrated here through both the model simulation approach
718 and experimental data.

719 Another important issue that requires attention is the potential effect of the spectral resolution
720 on the retrieval of fluorescence, which has been questioned by some authors (Damm et al.,
721 2014). To raising awareness on this issue, the spectral resolution of the hyperspectral sensor
722 used in this study (6.5 nm) was also analysed. Both, experimental and simulation analysis
723 demonstrated that the retrieval of fluorescence is feasible with such spectral resolution. SIF
724 accuracy retrievals are only slightly diminished by using a spectral resolution of 6.5 nm
725 compared with the effect produced by other factors such as forest structure and density. The
726 expected deviation between absolute SIF values retrieved at 1 nm and with 6.5 nm FWHM
727 (with high sampling intervals) do not likely affect the conclusions obtained in studies such as
728 this one, which focuses in fluorescence retrievals for stress detection purposes rather than the
729 absolute quantification of SIF values. In these studies, the variation of fluorescence in relative

730 terms enables the assessment of early stress related to disease severity levels and forest
731 decline variability.

732 Besides the intrinsic factors that modulate the SIF at the canopy level, the pixel aggregation
733 used affects the estimated intensity. In particular, the accuracy of SIF retrieved from
734 aggregated pixels beyond the crown level is uncertain because the pixel mixture may include
735 the confounding effects of shaded pixels and background soil, decreasing the absorption in
736 the O₂-B band, and therefore, the overall magnitude of the F-signal. A more refined 3-D
737 canopy model including physiological, aerodynamic and geometry variables would be needed
738 to better analyse the physiological regulation of the fluorescence yield as a function of
739 micrometeorological drivers. Nevertheless, the results of the present study showed a strong
740 improvement in the retrieval of SIF at the leaf level from coarse resolution pixels based on
741 the inversion of FluorFLIGHT accounting for structural variables ($r^2=0.70$) compared to the
742 results obtained ignoring those effects ($r^2=0.42$).

743 Therefore, these results suggest that the use of a 3-D RTM, such as FluorFLIGHT, may
744 improve the estimation of SIF at global scales. SIF estimation at the crown level becomes
745 particularly critical with invasive plant pathogens affecting individual trees alternately and
746 selectively within the forest canopy. This is the case of sudden oak death disease progression
747 at local and spatial scales (Ramage et al., 2012). Local patchiness in disease presence/severity
748 can be clearly observed with the high local variability of the F_i inversion map estimated at the
749 oak site. Hence, mapping fluorescence emission based on FluorFLIGHT model inversion
750 approaches sets a new standard in the early detection of stress effects towards precision
751 forestry. The early detection of hotspot locations (focus of infection or decline) might help to
752 combat forest decline processes, and in case of *Phytophthora* infections, prevent the spread of
753 the infection.

754 These results are of particular interest for the FLEX mission, approved as ESA's Earth
755 Explorer 8 (Drusch et al., 2016), which will with provide fluorescence emission at finer
756 spatial scale than currently possible, and potential to resolve full fluorescence emission
757 spectrum with further information on stress attribution (Ač et al., 2015; Cogliati et al., 2015).
758 There are still many challenges for measurement of SIF from space; further validation studies
759 need to be undertaken to assess modelling results and the effect of environmental stress
760 factors on ecophysiological traits and forest productivity. Another important issue that
761 requires attention is the potential application of these methods to different forest types
762 increasingly complex in terms of structure and tree species composition. The canopy
763 structure and spatial heterogeneity of the open-and-sparse oak woodland studied here may
764 have a different effect on global SIF estimates to other types of land covers: with higher
765 canopy density (closed forest canopies), with higher heterogeneity in species and/or soil
766 composition or higher vertical heterogeneity within forest canopies.

767 It is important to highlight the difficulties of validating the estimation of SIF from spaceborne
768 sensors over forest canopies, which encompass challenging experimental field campaigns and
769 sampling conditions. The use of very high resolution airborne hyperspectral imagery as used
770 in this and similar studies may be valuable. More studies supporting the validation of SIF are
771 foreseen to improve our understanding in the link between SIF and photosynthetic activity
772 with a greater degree of confidence. SIF retrievals using FluorFLIGHT should be further
773 validated for different types of canopies and physiological conditions for monitoring forest
774 decline processes.

775

776 **5. Conclusions.**

777 Measuring SIF remotely is potentially a valuable tool to track the health and productivity of
778 forest but also brings important challenges. This study gives the first 3-D model of canopy
779 fluorescence, combined with an original field campaign aimed at quantifying the link
780 between canopy physiology and detection at scales suitable for satellite remote sensing. The
781 results show a link between physiologically based indicators and SIF retrieval from
782 hyperspectral remote sensing for an oak forest affected by root pathogen infections and water
783 stress.

784 Model estimations against in-situ measurements conducted over the oak forest demonstrated
785 significant utility of SIF for precision physiological condition characterization. The
786 FluorFLIGHT model enabled the estimation of sunlit vegetation fluorescence from coarse
787 pixels ($r^2=0.79$, $p<0.01$) accounting for the large effects produced by the FC and canopy
788 structure. The model inversion approach at three steps, which progressively approximates the
789 observed canopy structure heterogeneity from the study sites, showed improvements in the
790 estimation of leaf-based fluorescence measurement.

791 The results presented in this study demonstrated the fluorescence signal retrieved from mixed
792 pixels is significantly affected by the effects caused by the illumination condition and the
793 structural component of the canopy ($r^2=0.42$). Those effects are intrinsic to all radiance
794 spectral retrieved from aggregated pixels irrespective of the sample size, but get increasingly
795 critical with increasing levels of aggregation (pixel size). In particular, the SIF signal was
796 significantly lower when retrieved from coarse pixels (lower than 10x10 m resolution) than
797 from sunlit pixel crowns (<50%). Fluorescence retrieval using FluorFLIGHT and accounting
798 for pixel aggregation minimized the impact of the canopy structure and other scene
799 components improving the accuracy of the estimations ($r^2=0.70$).

800

801 **Acknowledgements**

802 This study was conducted under the Marie Curie Intra-European Fellowship for Career
803 Development. Data collection was partially supported by the THERMOLIDAR FP7 Project
804 and the QUERCUSAT project from the Spanish funding agency "Ministerio de Economía y
805 Competitividad". The authors are most grateful to the Treesat research group (ERSAF,
806 University of Cordoba, Spain) for the support provided during the field campaigns.

807

808 **References**

- 809 Ač, A., Malenovský, Z., Olejníčková, J., Gallé, A., Rascher, U., Mohammed, G., 2015. Meta-
810 analysis assessing potential of steady-state chlorophyll fluorescence for remote sensing
811 detection of plant water, temperature and nitrogen stress. *Remote Sens. Environ.* 168,
812 420–436. doi:10.1016/j.rse.2015.07.022
- 813 Bye, I.J., North, P.R.J., Los, S.O., Kljun, N., Rosette, J.A.B., Hopkinson, C., Chasmer, L.,
814 Mahoney, C., 2017. Estimating forest canopy parameters from satellite waveform
815 LiDAR by inversion of the FLIGHT three-dimensional radiative transfer model.
816 *Remote Sens. Environ.* 188, 177-189. doi: 10.1016/j.rse.2016.10.048
- 817 Cogliati, S., Verhoef, W., Kraft, S., Sabater, N., Alonso, L., Vicent, J., Moreno, J., Drusch,
818 M., Colombo, R., 2015. Retrieval of sun-induced fluorescence using advanced spectral
819 fitting methods. *Remote Sens. Environ.* 169, 344–357. doi:10.1016/j.rse.2015.08.022
- 820 Damm, A., Guanter, L., Laurent, V.C.E., Schaepman, M.E., Schickling, A., Rascher, U.,
821 2014. FLD-based retrieval of sun-induced chlorophyll fluorescence from medium
822 spectral resolution airborne spectroscopy data. *Remote Sens. Environ.* 147, 256–266.
823 doi:10.1016/j.rse.2014.03.009

824 Damm, A., Guanter, L., Verhoef, W., Schläpfer, D., Garbari, S., Schaepman, M.E., 2015.
825 Impact of varying irradiance on vegetation indices and chlorophyll fluorescence
826 derived from spectroscopy data. *Remote Sens. Environ.* 156, 202–215.
827 doi:10.1016/j.rse.2014.09.031

828 Drusch, M., Moreno, J., Del Bello, U., Franco, R., Goulas, Y., Huth, A., Kraft, S., Middleton,
829 E. M., Miglietta, F., Mohammed, G., Nedbal, L., Rascher, U., Schüttemeyer, D.,
830 Verhoef, W., 2016. The FLuorescence EXplorer Mission Concept-ESA's Earth
831 Explorer 8. *IEEE Transactions on Geoscience and Remote Sensing* , vol. PP, (99), pp.1-
832 12. doi: 10.1109/TGRS.2016.2621820

833 Duffour, C., Olioso, A., Demarty, J., Van der Tol, C., Lagouarde, J.-P., 2015. An evaluation
834 of SCOPE: A tool to simulate the directional anisotropy of satellite-measured surface
835 temperatures. *Remote Sens. Environ.* 158, 362–375. doi:10.1016/j.rse.2014.10.019

836 Feret, J.-B., François, C., Asner, G.P., Gitelson, A.A., Martin, R.E., Bidel, L.P.R., Ustin,
837 S.L., le Maire, G., Jacquemoud, S., 2008. PROSPECT-4 and 5: Advances in the leaf
838 optical properties model separating photosynthetic pigments. *Remote Sens. Environ.*
839 112, 3030–3043. doi:10.1016/j.rse.2008.02.012

840 Ferraz, J., Casas, A.T., Caetano, P., 2000. El decaimiento y muerte de encinas en tres dehesas
841 de la provincia de Huelva. *Bol. Sanid. Veg. Plagas* 26, 447–464.

842 Franck, F., Juneau, P., Popovic, R., 2002. Resolution of the Photosystem I and Photosystem
843 II contributions to chlorophyll fluorescence of intact leaves at room temperature.
844 *Biochim. Biophys. Acta BBA - Bioenerg.* 1556, 239–246. doi:10.1016/S0005-
845 2728(02)00366-3

846 Frankenberg, C., Fisher, J.B., Worden, J., Badgley, G., Saatchi, S.S., Lee, J.-E., Toon, G.C.,
847 Butz, A., Jung, M., Kuze, A., Yokota, T., 2011. New global observations of the
848 terrestrial carbon cycle from GOSAT: Patterns of plant fluorescence with gross primary
849 productivity. *Geophys. Res. Lett.* 38, L17706. doi:10.1029/2011GL048738

850 Gamon, J.A., Peñuelas, J., Field, C.B., 1992. A narrow-waveband spectral index that tracks
851 diurnal changes in photosynthetic efficiency. *Remote Sensing of Environment* 41, 35–
852 44. doi:10.1016/0034-4257(92)90059-S

853 Genty, B., Briantais, J.-M., Baker, N.R., 1989. The relationship between the quantum yield of
854 photosynthetic electron transport and quenching of chlorophyll fluorescence. *Biochim.*
855 *Biophys. Acta BBA - Gen. Subj.* 990, 87–92. doi:10.1016/S0304-4165(89)80016-9

856 Guanter, L., Frankenberg, C., Dudhia, A., Lewis, P.E., Gómez-Dans, J., Kuze, A., Suto, H.,
857 Grainger, R.G., 2012. Retrieval and global assessment of terrestrial chlorophyll
858 fluorescence from GOSAT space measurements. *Remote Sens. Environ.* 121, 236–251.
859 doi:10.1016/j.rse.2012.02.006

860 Hernández-Clemente, R., Navarro-Cerrillo, R.M., Suarez, L., Morales, F., Zarco-Tejada, P.J.,
861 2011. Assessing structural effects on PRI for stress detection in conifer forests. *Remote*
862 *Sens. Environ.* 115, 2360–2375. doi:10.1016/j.rse.2011.04.036

863 Hernández-Clemente, R., Navarro-Cerrillo, R. M., Ramírez, F.J.R., Hornero, A., Zarco-
864 Tejada, P.J. 2014. A Novel Methodology to Estimate Single-Tree Biophysical
865 Parameters from 3-D Digital Imagery Compared to Aerial Laser Scanner Data. *Remote*
866 *Sensing*, 6, 11, 11627–11648. doi: 10.3390/rs61111627

867 Jacquemoud, S., Baret, F., 1990. PROSPECT: A model of leaf optical properties spectra.
868 *Remote Sens. Environ.* 34, 75–91. doi:10.1016/0034-4257(90)90100-Z

869 Joiner, J., Yoshida, Y., Vasilkov, A.P., Schaefer, K., Jung, M., Guanter, L., Zhang, Y.,
870 Garrity, S., Middleton, E.M., Huemmrich, K.F., Gu, L., Belelli Marchesini, L., 2014.
871 The seasonal cycle of satellite chlorophyll fluorescence observations and its
872 relationship to vegetation phenology and ecosystem atmosphere carbon exchange.
873 Remote Sens. Environ. 152, 375–391. doi:10.1016/j.rse.2014.06.022

874 Kraft, S., Bello, U.D., Bouvet, M., Drusch, M., Moreno, J., 2012. FLEX: ESA's Earth
875 Explorer 8 candidate mission, in: 2012 IEEE International Geoscience and Remote
876 Sensing Symposium. Presented at the 2012 IEEE International Geoscience and Remote
877 Sensing Symposium, pp. 7125–7128. doi:10.1109/IGARSS.2012.6352020

878 Krause, G.H., Weis, E., 1984. Chlorophyll fluorescence as a tool in plant physiology.
879 Photosynth. Res. 5, 139–157. doi:10.1007/BF00028527

880 Kuze, A., Suto, H., Nakajima, M., Hamazaki, T., 2009. Thermal and near infrared sensor for
881 carbon observation Fourier-transform spectrometer on the Greenhouse Gases
882 Observing Satellite for greenhouse gases monitoring. Appl. Opt. 48, 6716–6733.

883 Larbi, A., Abadía, A., Morales, F., Abadía, J., 2004. Fe Resupply to Fe-deficient Sugar Beet
884 Plants Leads to Rapid Changes in the Violaxanthin Cycle and other Photosynthetic
885 Characteristics without Significant de novo Chlorophyll Synthesis. Photosynth. Res.
886 79, 59–69. doi:10.1023/B:PRES.0000011919.35309.5e

887 Leonenko, G., Los, S.O., North, P.R.J., 2013. Statistical Distances and Their Applications to
888 Biophysical Parameter Estimation: Information Measures, M-Estimates, and Minimum
889 Contrast Methods. Remote Sens. 5, 1355–1388. doi:10.3390/rs5031355

890 Maurel, M., Robin, C., Capron, G., Desprez-Loustau, M.-L., 2001. Effects of root damage
891 associated with *Phytophthora cinnamomi* on water relations, biomass accumulation,

892 mineral nutrition and vulnerability to water deficit of five oak and chestnut species. For.
893 Pathol. 31, 353–369. doi:10.1046/j.1439-0329.2001.00258.x

894 Miller, J., 2005. Development of a Vegetation Fluorescence Canopy Model.

895 Moralejo, E., García-Muñoz, J.A., Descals, E., 2009. Susceptibility of Iberian trees to
896 *Phytophthora ramorum* and *P. cinnamomi*. Plant Pathol. 58, 271–283.
897 doi:10.1111/j.1365-3059.2008.01956.x

898 Natalini, F., Alejano, R., Vázquez-Piqué, J., Cañellas, I., Gea-Izquierdo, G., 2016. The role of
899 climate change in the widespread mortality of holm oak in open woodlands of
900 Southwestern Spain. Dendrochronologia 38, 51–60. doi:10.1016/j.dendro.2016.03.003

901 Naumann, J.C., Anderson, J.E., Young, D.R., 2008. Linking physiological responses,
902 chlorophyll fluorescence and hyperspectral imagery to detect salinity stress using the
903 physiological reflectance index in the coastal shrub, *Myrica cerifera*. Remote Sens.
904 Environ. 112, 3865–3875. doi:10.1016/j.rse.2008.06.004

905 North, P., 1996. Three-dimensional forest light interaction model using a Monte Carlo
906 method. IEEE Trans. Geosci. Remote Sens. 34, 946–956. doi:10.1109/36.508411

907 North, P.R.J., Rosette, J.A.B., Suárez, J.C., Los, S.O., 2010. A Monte Carlo radiative transfer
908 model of satellite waveform LiDAR. Int. J. Remote Sens. 31, 1343–1358.
909 doi:10.1080/01431160903380664

910 Pedrós, R., Moya, I., Goulas, Y., Jacquemoud, S., 2008. Chlorophyll fluorescence emission
911 spectrum inside a leaf. Photochem. Amp Photobiol. Sci. Off. J. Eur. Photochem. Assoc.
912 Eur. Soc. Photobiol. 7, 498–502. doi:10.1039/b719506k

- 913 Prieto-Blanco, A., North, P.R.J., Barnsley, M.J., Fox, N., 2009. Satellite-driven modelling of
914 Net Primary Productivity (NPP): Theoretical analysis. *Remote Sens. Environ.* 113,
915 137–147. doi:10.1016/j.rse.2008.09.002
- 916 Ramage, B.S., Forrestel, A.B., Moritz, M.A., O’Hara, K.L., 2012. Sudden oak death disease
917 progression across two forest types and spatial scales. *J. Veg. Sci.* 23, 151–163.
918 doi:10.1111/j.1654-1103.2011.01340.x
- 919 Roig Gómez, S., Ponce, R.A., González Sánchez, M., García del Barrio, J.M., Cañellas Rey
920 de Viñas, I., 2007. Caracterización de la dehesa española de encina y alcornoque a
921 partir del inventario forestal nacional. *Cuad. Soc. Esp. Cienc. For.* 163–170.
- 922 Rossini, M., Nedbal, L., Guanter, L., Ač, A., Alonso, L., Burkart, A., Cogliati, S., Colombo,
923 R., Damm, A., Drusch, M., Hanus, J., Janoutova, R., Julitta, T., Kokkalis, P., Moreno,
924 J., Novotny, J., Panigada, C., Pinto, F., Schickling, A., Schüttemeyer, D., Zemek, F.,
925 Rascher, U., 2015. Red and far red Sun-induced chlorophyll fluorescence as a measure
926 of plant photosynthesis. *Geophys. Res. Lett.* 42, 2014GL062943.
927 doi:10.1002/2014GL062943
- 928 Rouse, J.W., Jr., Haas, R.H., Schell, J.A., Deering, D.W., 1974. Monitoring Vegetation
929 Systems in the Great Plains with ERTS. *NASA Spec. Publ.* 351, 309.
- 930 Scholander, P.F., Bradstreet, E.D., Hemmingsen, E.A., Hammel, H.T., 1965. Sap Pressure in
931 Vascular Plants. *Science* 148, 339–346. doi:10.1126/science.148.3668.339
- 932 Thayer, S.S., Björkman, O., 1990. Leaf Xanthophyll content and composition in sun and
933 shade determined by HPLC. *Photosynth. Res.* 23, 331–343. doi:10.1007/BF00034864

934 van der Tol, C., Verhoef, W., Timmermans, J., Verhoef, A., Su, Z., 2009. An integrated
935 model of soil-canopy spectral radiances, photosynthesis, fluorescence, temperature and
936 energy balance. *Biogeosciences* 6, 3109–3129. doi:10.5194/bg-6-3109-2009

937 Van Wittenberghe, S., Alonso, L., Verrelst, J., Hermans, I., Valcke, R., Veroustraete, F.,
938 Moreno, J., Samson, R., 2014. A field study on solar-induced chlorophyll fluorescence
939 and pigment parameters along a vertical canopy gradient of four tree species in an
940 urban environment. *Sci. Total Environ.* 466–467, 185–194.
941 doi:10.1016/j.scitotenv.2013.07.024

942 Van Wittenberghe, S., Alonso, L., Verrelst, J., Moreno, J., Samson, R., 2015. Bidirectional
943 sun-induced chlorophyll fluorescence emission is influenced by leaf structure and light
944 scattering properties — A bottom-up approach. *Remote Sens. Environ.* 158, 169–179.
945 doi:10.1016/j.rse.2014.11.012

946 Verhoef, W., 2004. Extension of SAIL to model solar - induced canopy fluorescence spectra.
947 Presented at the Proceedings of the 2nd international workshop on remote sensing of
948 vegetation fluorescence, Paris : ESA, 2004. (ESA WPP ; 242), Montreal, Canada, p.
949 18p.

950 Verrelst, J., Rivera, J.P., van der Tol, C., Magnani, F., Mohammed, G., Moreno, J., 2015.
951 Global sensitivity analysis of the SCOPE model: What drives simulated canopy-leaving
952 sun-induced fluorescence? *Remote Sens. Environ.* 166, 8–21.
953 doi:10.1016/j.rse.2015.06.002

954 Verrelst, J., van der Tol, C., Magnani, F., Sabater, N., Rivera, J.P., Mohammed, G., Moreno,
955 J., 2016. Evaluating the predictive power of sun-induced chlorophyll fluorescence to

956 estimate net photosynthesis of vegetation canopies: A SCOPE modeling study. *Remote*
957 *Sens. Environ.* 176, 139–151. doi:10.1016/j.rse.2016.01.018

958 Vilfana, N., van der Tol, C., Muller, O., Rascher, U., Verhoef, W., 2016. Fluspect-B: A
959 model for leaf fluorescence, reflectance and transmittance spectra. *Remote Sens.*
960 *Environ.* 186, 596–615. doi: 10.1016/j.rse.2016.09.017

961 Widlowski, J.-L., Taberner, M., Pinty, B., Bruniquel-Pinel, V., Disney, M., Fernandes, R.,
962 Gastellu-Etchegorry, J.-P., Gobron, N., Kuusk, A., Lavergne, T., Leblanc, S., Lewis,
963 P.E., Martin, E., Möttus, M., North, P.R.J., Qin, W., Robustelli, M., Rochdi, N.,
964 Ruiloba, R., Soler, C., Thompson, R., Verhoef, W., Verstraete, M.M., Xie, D., 2007.
965 Third Radiation Transfer Model Intercomparison (RAMI) exercise: Documenting
966 progress in canopy reflectance models. *J. Geophys. Res. Atmospheres* 112, D09111.
967 doi:10.1029/2006JD007821

968 Widlowski, J.-L., Robustelli, M., Disney, M., Gastellu-Etchegorry, J.-P., Lavergne, T.,
969 Lewis, P., North, P.R.J., Pinty, B., Thompson, R., Verstraete, M.M., 2008. The RAMI
970 On-line Model Checker (ROMC): A web-based benchmarking facility for canopy
971 reflectance models. *Remote Sens. Environ.* 112, 1144–1150.
972 doi:10.1016/j.rse.2007.07.016

973 Widlowski, J.-L., Mio, C., Disney, M., Adams, J., Andredakis, I., Atzberger, C., Brennan, J.,
974 Busetto, L., Chelle, M., Ceccherini, G., Colombo, R., Côté, J.-F., Eemäe, A., Essery,
975 R., Gastellu-Etchegorry, J.-P., Gobron, N., Grau, E., Haverd, V., Homolová, L., Huang,
976 H., Hunt, L., Kobayashi, H., Koetz, B., Kuusk, A., Kuusk, J., Lang, M., Lewis, P.E.,
977 Lovell, J.L., Malenovský, Z., Meroni, M., Morsdorf, F., Möttus, M., Ni-Meister, W.,
978 Pinty, B., Rautiainen, M., Schlerf, M., Somers, B., Stuckens, J., Verstraete, M.M.,
979 Yang, W., Zhao, F., Zenone, T., 2015. The fourth phase of the radiative transfer model

980 intercomparison (RAMI) exercise: Actual canopy scenarios and conformity testing.
981 Remote Sens. Environ. 169, 418–437. doi:10.1016/j.rse.2015.08.016

982 Zarco-Tejada, P.J., Miller, J.R., Noland, T.L., Mohammed, G.H., Sampson, P.H., 2001.
983 Scaling-up and model inversion methods with narrowband optical indices for
984 chlorophyll content estimation in closed forest canopies with hyperspectral data. IEEE
985 Trans. Geosci. Remote Sens. 39, 1491–1507. doi:10.1109/36.934080

986 Zarco-Tejada, P., Berjon, A., Lopezlozano, R., Miller, J., Martin, P., Cachorro, V., Gonzalez,
987 M., de Frutos, A., 2005. Assessing vineyard condition with hyperspectral indices: Leaf
988 and canopy reflectance simulation in a row-structured discontinuous canopy. Remote
989 Sens. Environ. 99, 271–287. doi:10.1016/j.rse.2005.09.002

990 Zarco-Tejada, P.J., Catalina, A., González, M.R., Martín, P., 2013a. Relationships between
991 net photosynthesis and steady-state chlorophyll fluorescence retrieved from airborne
992 hyperspectral imagery. Remote Sens. Environ. 136, 247–258.
993 doi:10.1016/j.rse.2013.05.011

994 Zarco-Tejada, P.J., Suarez, L., Gonzalez-Dugo, V., 2013b. Spatial Resolution Effects on
995 Chlorophyll Fluorescence Retrieval in a Heterogeneous Canopy Using Hyperspectral
996 Imagery and Radiative Transfer Simulation. IEEE Geosci. Remote Sens. Lett. 10, 937–
997 941. doi:10.1109/LGRS.2013.2252877

998 Zarco-Tejada, P.J., Morales, A., Testi, L., Villalobos, F.J., 2013c. Spatio-temporal patterns of
999 chlorophyll fluorescence and physiological and structural indices acquired from
1000 hyperspectral imagery as compared with carbon fluxes measured with eddy covariance.
1001 Remote Sens. Environ. 133, 102–115. doi:10.1016/j.rse.2013.02.003

1002 Zarco-Tejada, P.J., González-Dugo, M.V., Fereres, E., 2016. Seasonal stability of chlorophyll
1003 fluorescence quantified from airborne hyperspectral imagery as an indicator of net
1004 photosynthesis in the context of precision agriculture. *Remote Sens. Environ.* 179, 89–
1005 103. doi:10.1016/j.rse.2016.03.024

1006

1007 **List of Figure captions**

1008 **Fig. 1.** Airborne hyperspectral flight line acquired with the micro-hyperspectral imager
1009 yielding 60 cm resolution (a), oak forest study site and tree crowns selected for the
1010 quantification of SIF (b), high resolution spectral reflectance extracted from sunlit and
1011 shadowed crown and soil components (c).

1012 **Fig. 2.** Example of a 30x30 m scene (highlighted squared) of the micro-hyperspectral
1013 imagery acquired at 40 cm resolution in color-infrared (a) and sunlit and shadowed
1014 component identification of the crown on the micro-hyperspectral imagery (b). Example of a
1015 30x30 m scene (highlighted squared) simulated with FluorFLIGHT (c) and sunlit and
1016 shadowed component identification on simulated images (d).

1017 **Fig. 3.** Example of the spectral radiance extracted from the micro-hyperspectral image (a)
1018 and from FluorFLIGHT simulated radiance (L) (b) for different scene components: sunlit
1019 crown, full crown, sunlit soil, shadowed soil and aggregated pixels (30x30 m) in the O2-A
1020 feature used for fluorescence quantification. Spectral features extracted from Fig. 2.

1021 **Fig. 4.** Subplots emulating the aggregation effects due to the spatial resolution overlaid onto
1022 the micro-hyperspectral imagery acquired at 60 cm resolution (a) and a FluorFLIGHT
1023 simulated image (b), both in colour-infrared. F (FLD3) variation based on the hyperspectral
1024 image (c) and the simulated image (d) estimated from: sunlit pixels of the crown (SL crown),
1025 shadowed pixels of the crown (SW crown), full crown pixels (crown=SL+SW) and eighteen
1026 aggregated pixels from a 5x5 m window to a 100x100 m window.

1027 **Fig. 5.** Simulated canopy radiance including the effects of fluorescence using the
1028 FluorFLIGHT model for a varied range of leaf area index (LAI) (0.5-4.5) (a) and fractional
1029 cover (FC) (15-65%) (b). Fluorescence quantum yield efficiency at photosystem level

1030 ($F_i=0.06$). All other input parameters of the model were set using nominal values included in
1031 Table 1.

1032 **Fig. 6.** Overview of the processing steps followed in the retrieval of sun-induced fluorescence
1033 (SIF) showing the input variables used for the simulations. Inputs description included in
1034 Table 1.

1035 **Fig. 7.** Relationship between de-epoxidation state of the xanthophyll cycle (DEPS) (a) and
1036 water potential (b) against F (FLD3) from sunlit pixel radiance L retrieved from the
1037 hyperspectral image. Relationships between steady-state fluorescence yield (F_s) ground-data
1038 measurements of 15 oak trees and airborne-based F (FLD3) retrieved from sunlit pixel
1039 radiance (c) and 30x30 m aggregated pixels radiance (L) retrieved from the hyperspectral
1040 image (d). Trees with higher and lower level of affectation are highlighted within a dashed
1041 grey and black line respectively.

1042 **Fig. 8.** Effects of forest structural variables on simulated canopy fluorescence (FLD3) as a
1043 function of LAI (0-5) at the crown level (a) and fractional cover FC (10-90%) at the canopy
1044 level (b). All other input parameters of the model were set using nominal values included in
1045 Table 1.

1046 **Fig. 9.** Relationships between FluorFLIGHT simulations of canopy L obtained from sunlit
1047 crown pixels and full crowns as a function of LAI (1-4) (a). Relationships between
1048 FluorFLIGHT simulations of crown L obtained from sunlit crowns and aggregated pixels as a
1049 function of FC (10-90%) (b).

1050 **Fig. 10.** Comparison of FluorFLIGHT model-based fluorescence quantum efficiency (F_i) and
1051 F (FLD3) retrieved from shaded and sunlit crown pixels, full crown pixels and aggregated
1052 pixels as a function of LAI (0-4) and FC (0-100%).

1053 **Fig 11.** Relationships between the simulated FluorFLIGHT fluorescence quantum efficiency
1054 retrieved (FLD3 method) from synthetic spectra retrieved from 30x30 m aggregated pixels
1055 (a), full crown pixels (b) and sunlit crown pixels at 6.5 nm (c) and at 1 nm (d). LAI (0-4) and
1056 FC (40-60%). All other input parameters of the model were set using nominal values
1057 included in Table 1.

1058 **Fig. 12.** (a) Sunlit and shadowed component identification of the crown on the micro-
1059 hyperspectral imagery. (b) SIF map showing different values between sunlit and shaded
1060 crown F (FLD3).

1061 **Fig. 13.** Relationships between F_s ground-data measurements and fluorescence estimations
1062 retrievals using FluorFLIGHT applied to aggregated pixels without accounting for pixel
1063 aggregation (30x30 m aggregated pixels) and accounting for pixel aggregation (full crown
1064 pixels) with FluorFLIGHT (a) Leaf level relationship between F_s ground-data measurements
1065 and fluorescence quantum yield estimated with FluorFLIGHT (b).

1066 **Fig. 14.** F_i retrieval at the crown level estimated from the 60-cm hyperspectral image using
1067 the fluorescence in-filling method F (FLD3) within the oak forest.

1068 **Table 1.** Ground truth data collected and optical measurements.

1069 **Table 2.** Nominal values and range of variation used in FluorFLIGHT simulation analysis
1070 based on field data measurements.

1071 **Table 3.** Correlation coefficient R between steady-state fluorescence yield (F_s), de-
1072 epoxidation state of the xanthophyll cycle (DEPS) and water potential (ψ) and crown-based
1073 spectral vegetation indices, including structural and physiological vegetation indices.

1074